2012

# A Hydraulic Analysis of the Long Crossover Passage in a Multi-Stage Pump

Alexander Hernandez
*Lehigh University*

# A Hydraulic Analysis of the Long Crossover Passage in a Multi-Stage Pump

by

Alexander Hernandez

A Thesis

Presented to the Graduate and Research Committee

of Lehigh University

in Candidacy for the Degree of

Master of Science

in

Mechanical Engineering and Mechanics

Lehigh Univeristy

December 2011

This thesis is accepted and approved in partial fulfillment of the requirements for the Master of Science.

_____
Date

_____
Alparslan Oztekin
Thesis Advisor

_____
D. Gary Harlow
Department Chair

## Acknowledgements

I would like to extend my gratitude to the managers and employees at Flowserve Corporation who have taken the time to support my educational efforts. Special thanks go out to Tim Wotring, Mark O'Sullivan, John Lawler and Dr. Paul Cooper specifically.

Special thanks also to the Lehigh University faculty, specifically Dr. Robert Lucas for being my undergraduate advisor and Dr. Alparslan Oztekin for being my doctoral advisor.

Finally, this report is dedicated to my family, whose support for my education has never wavered. Without you this never would have been finished.

# Table of Contents

## List of Tables

## List of Figures

## Abstract

In response to market demands, Flowserve Corporation is investigating methods for reducing hydraulic losses in certain pumps. After being manufactured and tested, a recent crossover design was seen to be a great improvement over the typical design. This crossover passage was modeled and analyzed using CFD in order to identify further areas for improvement. The Reynold's Averaged Navier-Stokes (RANS) equations are solved using the k-ε turbulence model. The velocity and pressure fields were simulated in the passage as well as the shear stress along the walls. The velocity and pressure fields are plotted at several cross-sections. It is shown here that total pressure drop of only 1.2% is predicted from the inlet to the outlet of the new crossover design. This is considered to be a significant performance improvement to these pumps. It is also noted that the low shear flow region is on the inner part of the bends. Secondary flows were identified in the areas of the passage with the highest curvature, but their effect on losses is minimal since the velocity pressure is shown to be only accounts about 10% of the total pressure. The new design was seen to be very well designed with minimal areas for improvement, specifically straightening the flow exiting the crossover passage. It is also shown that the significant level of swirl is passed into the suction volute of the succeeding impeller. That could impede the hydraulic efficiency of the next impeller. Future studies are planned to write a crossover generating program for future pumps of this type at varying specific speeds ($\Omega_S$).

# 1 Introduction

## *1.1 Problem Statement & Motivation*

Flowserve Corporation is a world leader in fluid motion and control equipment. Recent customer demand in the salt water reverse osmosis (SWRO) industry has driven the engineers to review one of the centrifugal pump lines to identify areas that can be modified for increased hydraulic efficiency in an effort to save energy and reduce process costs for the end user.

Due to the original design intent of this pump line, that of ease of manufacturing and minimal production costs, the existing crossover geometry design of the pump line was not optimized for hydraulic efficiency because the resulting shape would have been more costly to cast. Recent advances in SWRO technology have made larger water purification plants more economically feasible, but they still consume large amounts of energy to desalinate the seawater. In order to become a major provider for the necessary seawater injection pumps, Flowserve is modifying the design intent of large pumps in this pump line. Specifically, those pumps that are appropriately sized to pressurize the seawater to its osmotic pressure are being evaluated to maximize their hydraulic efficiency. Initial test results of a recent design have shown efficiency improvements. CFD and other analytical tools were then commissioned to evaluate this recent design and propose modifications to further increase the hydraulic efficiency of new pumps.

## *1.2 Background*

When designing pumps, the parameters of primary interest are the volumetric flow, Q, the running speed, ω, and the generated energy per unit mass (in the form of both velocity and static pressure), gH. Applying Buckingham Pi theory to these parameters yields:

$$[Q] = {}^{L^3}/_{t}, [\omega] = {}^{1}/_{t}, [gH] = {}^{L^2}/_{t^2}$$

$$\Pi_1 = Q^{\alpha}(gH)^{\beta}\omega = L^0 t^0$$

$$3\alpha + 2\beta = 0$$
$$-\alpha - 2\beta - 1 = 0$$
$$\alpha = {}^{1}/_{2}$$
$$\beta = -{}^{3}/_{4}$$

$$\Pi_1 = \Omega_S = \frac{\omega\sqrt{Q}}{(gH)^{3/4}}$$

The above dimensionless parameter is known as the specific speed in the pump industry and more often written as:

$$N_S = \frac{N\sqrt{Q}}{H^{3/4}}$$

Because it was derived before Buckingham's modeling theory article was published (Buckingham, 1915). For the purposes of this paper, however, the classical dimensionless value $\Omega_S$ will be used. The pump in question has a $\Omega_S$ of .641.

The specific speed is important because it is the relationship between the kinetic (velocity) and potential (pressure) energy contained in the fluid stream. Pumps

of similar specific speeds can be considered to be dynamically similar and their impellers geometrically similar. This allows a single proven design to be scaled geometrically while keeping confidence in the expected performance of the final product. It should be noted that the results presented are only valid for similarly designed pumps of the same specific speed. Further investigation of other specific speeds will be necessary to apply these results to the entire line of pumps.

The pump line of interest is a multistage pump with large double volute collector geometry at the outlet of the impellers.

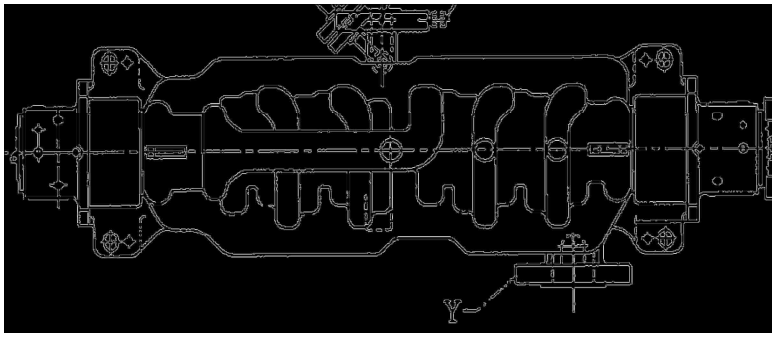

**Figure 1 - Top View of Original Design (©Flowserve Corp., 2000)**

In this pump line, the impellers are installed facing opposite directions in order to balance the axial thrust generated by the rotating element. This arrangement requires a long crossover passage that traverses approximately half of the length of the pump.

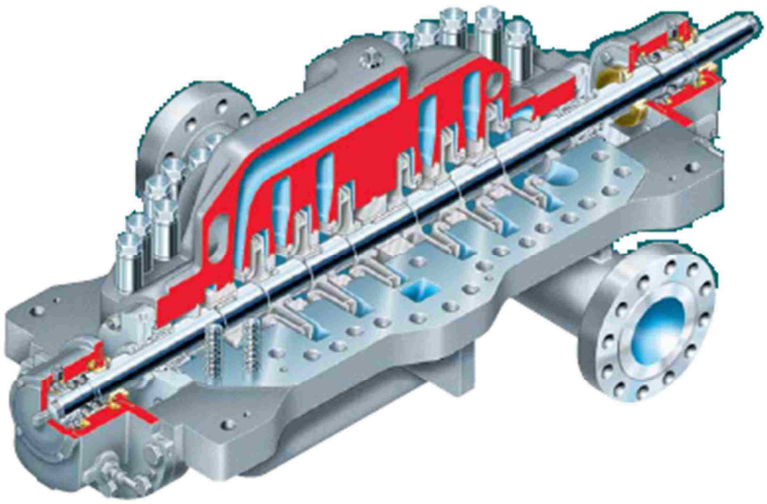

Figure 2 - Cross-Section of Typical Pump Offering (©Flowserve, 2009)

The standard design uses three short abrupt turns to direct the flow from one stage to the next.

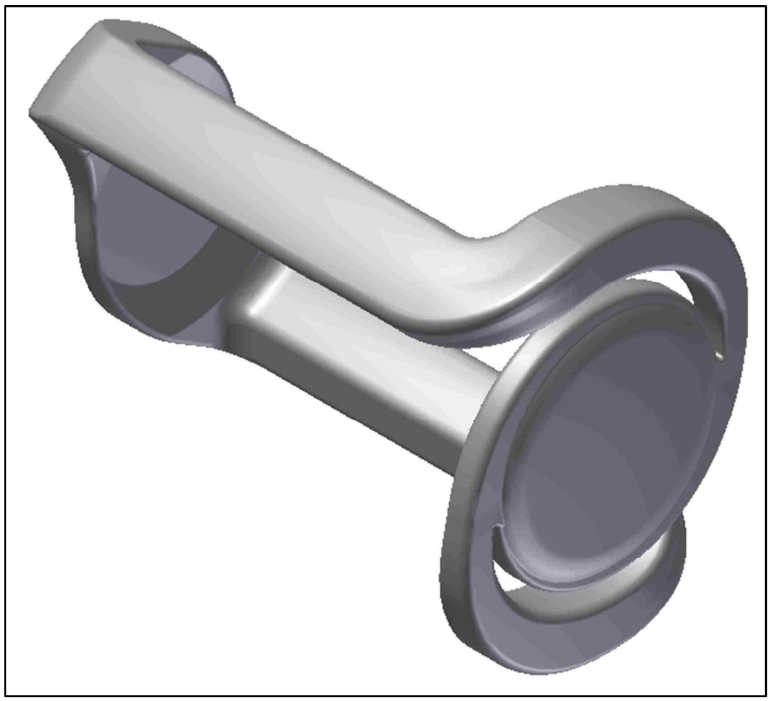

Figure 3 - Typical Long Crossover Design (©Flowserve, 2011)

Figure 1 is a typical top view of this arrangement. Note the long crossover spanning half of the pump with a sharp 90º turn midway along the pump axis and the sudden dump to the entrance of the furthest left stage. It is known that this creates secondary flows within the passage which lead to energy losses and lower efficiency (Miller, 1990).

In response to this, a long crossover was developed using a more gradual bend. This new design tested favorably and was accepted by the customer. The aim of this study was to use CFD to identify other areas of interest in the long crossover and its interaction with the collector volute that can be improved upon to further improve hydraulic efficiency while keeping manufacturing costs as low as possible.

### *1.3 Physical Concepts*

The long crossover of the pump is essentially a diffusor that transitions into a bent elbow which then transitions into a nozzle. This being the case, the theory for flow in curved passages must be coupled with the theory for diffusors and nozzles. According to Lobanoff & Ross, the principal functions of a crossover are as follows:

- To convert the velocity head at the volute throat into pressure as soon as possible, thereby minimizing the overall pressure losses in the crossover.
- To turn the flow 180º from the exit of one stage into the suction of the next.
- To deliver a uniformly distributed flow to the eye of the succeeding impeller.
- To accomplish all these functions with minimum losses at minimum cost (Lobanoff & Ross, 1992).

Stepanoff also states that for efficient operation, the first three functions above should be performed independently or one at a time. This is because velocity cannot be efficiently converted to pressure while turning because higher velocity will simply migrate to the outside of the curve and not get converted; thus diffusion should be performed in a straight passage before the flow is turned (Stepanoff, 1993).

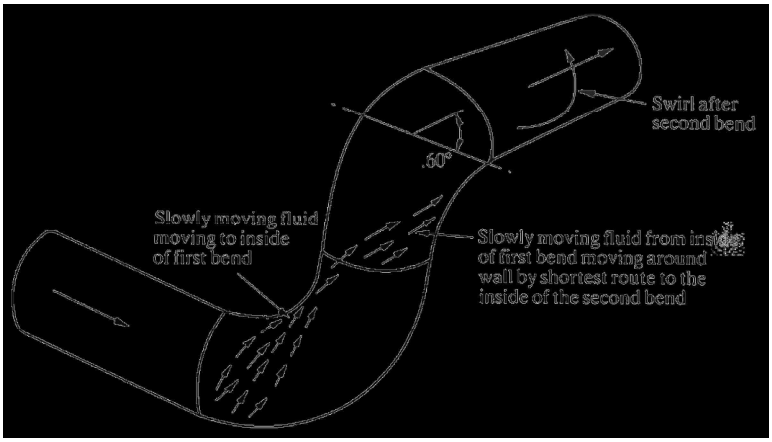


**Figure 4 - Secondary Flow Development in Bends (Miller, 1990)**

Miller identifies two primary sources of pressure losses; turbulence and adverse gradients (Miller, 1990). Turbulent flow in a pump is dominated by eddies of various sizes and length scales. These scales can vary from small, energetic eddies near the viscous sub-layer to large, elongated eddies in the low shear stress free stream. The turbulent eddies are three-dimensional and require a continuous supply of energy to maintain, or else they decay rapidly due to the viscous interaction of the fluid particles. This energy is taken from the flow in the form of shear forces. Smaller eddies near the boundary layer and any discontinuities such as wakes and zones of separation are immediately dissipated. Larger eddies dissipate their energy via the

process of cascading down to smaller eddies which are eventually completely dissipated by viscous forces in the fluid (Miller, 1990). This energy dissipation, of course, lowers the total energy of the fluid, resulting in a decrease of the hydraulic efficiency of the pump vis-à-vis the flow passage.

The direction of the pressure change is influential in the energy dissipation of the fluid. Static pressure can be converted to velocity (i.e. accelerated) very efficiently, but the same cannot be said for the reverse process (i.e. deceleration). The reason for this irreversibility lies in the non-uniformity of the velocity field as opposed to the uniformity of a static pressure field (Miller, 1990).

In a straight pipe with fully developed turbulent flow, for example, the velocity profile is not uniform, but greater along the center of the pipe and approaching zero at the wall. The static pressure, however, is virtually constant. The energy required to continue moving down the passage is proportional to the square of the velocity. This energy requirement for the entire passage, then, is based on the square of the mean velocity of the fluid. It is known, however, that the flow near the wall is significantly less than the free-stream velocity. This means that the flow near the wall will require additional energy by means of shear force transfer from the higher energy flow in the free stream, or else it will stall causing a separation at the wall (Miller, 1990).

In a diffusor the diverging walls are “pulling away” from the mean velocity direction. Thus the adjacent streams must be diverging from the straight flow in the center of the passage. This means that the energy transfer, which is solely due to shear

forces, begins to acquire a component normal to the streamlines that acts in the direction away from the wall. This skewed energy transfer direction causes the near-wall streamlines to essentially peel away from the wall, inducing a pocket of stagnation against the wall, which in turn is seen as separation. The resulting eddies that form near the walls dissipate the flow's energy so as to reattach it to the wall.

The reverse process is obviously much more efficient because the converging passage means that the normal component of the energy transfer is creating a high pressure (i.e. low velocity) fluid layer. This leaves the rest of the energy in the flow, which in turn speeds up the mean velocity as it accelerates down the nozzle. Essentially, the flow near the wall needs to give up its energy in order to develop the aforementioned velocity profile. This energy is readily given up to the free stream and the mean velocity is increased according to continuity. The nature of the losses in this case is also reduced because losses associated with pressure increase linearly rather than exponentially. This energy conversion can be seen as "pushing" the flow down the center of the pipe versus the diffusion process, which is more analogous to the free-stream "pulling" the near-wall flow along the periphery of the pipe. Following this mentality, the theories for diffusors, curved passages, and nozzles will be addressed in that order.

A diffusor is a channel that converts the kinetic (velocity) energy in a fluid stream into potential (static pressure) energy. It does so by gradually increasing the flow area so as to decelerate the flow.

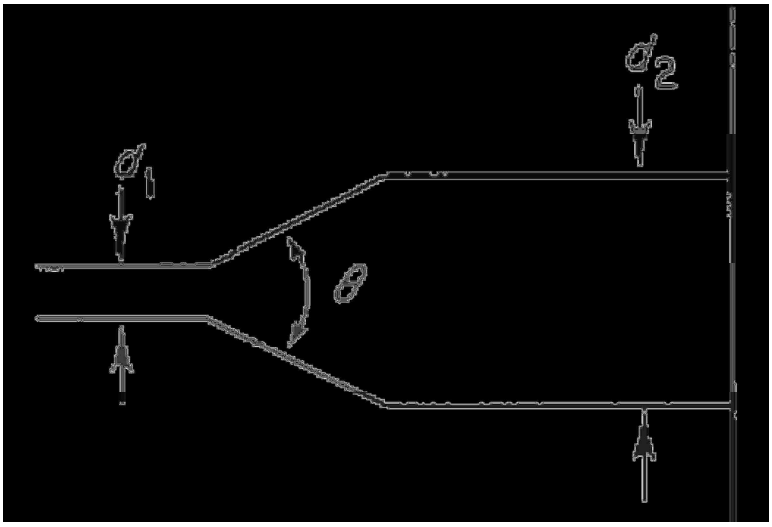


**Figure 5 - Typical Diffusor (Douglas, 1979)**

The total loss across the diffusor is made up of fluid friction along the length of the diffusor, which increases as the included angle, θ, approaches a straight pipe (0º), and separation losses, which increase as θ approaches a sudden expansion (180º) (Douglas, 1979). If separation occurs, localized pockets of high pressure form, upsetting the fluid stream and dissipating energy. The majority of hydraulic losses in a turbomachine such as a centrifugal pump are due to separation in all of its components, not just in the diffusor. In order for the reduction in velocity to occur as efficiently as possible, the flow must stay attached. If the flow separates, the main flow in the free stream will form a jet, causing turbulence in the separation zone that will dissipate energy as it resolves itself back into the free stream (Dunn, 2009). This is why large boundary layers are undesirable in diffusion; the faster stream will separate the flow if the diffusion is not gradual enough while a thinner boundary layer allows for more diffusion (Wilson, 1984).

Conceptually, the fluid molecules in the free stream can travel faster than those near a wall because there is nothing around them to impede their movement. As a near-wall molecule travels along the wall, it slows down and the molecules behind it must go around it. The only way for these molecules to pass the original is to leave the proximity of the wall, thus separating the flow from the wall. Similarly, as this molecule is slowed by its proximity to a static object, the adjacent molecules slow down due to their proximity to the first molecule. The energy lost by the deceleration of the adjacent molecules is transferred to the near-wall molecule to ensure that it remains in the fluid stream. If the energy is not enough to overcome the friction force with the wall, the molecule slows down to a stop and the previously described separation process is initiated.

From this explanation, it is easily seen why laminar flow is so susceptible to separation. The viscous drag forces on the boundary layer are small, so a small amount of diffusion is enough to overcome them and cause separation. Turbulent flow, on the other hand, has a constantly changing boundary layer interface where higher energy molecules in the free stream replace the molecules with the dissipated energy levels through eddies. This causes a smaller boundary layer and a more uniform velocity profile, at the expense of energy due to eddy dissipation and energy exchange at the near-wall flow. In the case of diffusion, however, the net energy loss due to this exchange results in an overall gain (i.e. smaller loss) relative to the purely laminar case.

The separation can occur at varying magnitudes. Gülich describes four different regimes:

A. Attached flow where the flow remains adjacent to the walls and diffuses as one would desire.
B. Intermittent separation where the boundary layer thickness slowly increases to a point where it cannot locally maintain its size and a small separation zone occurs, returning the boundary layer thickness back to its attached state.
C. One-sided separation where the flow decelerates enough to completely separate from a wall. This deflects the flow direction, allowing the boundary layer on the opposite wall to remain attached.
D. Two-sided separation where the flow detaches from both wall, forming a jet down the center of the channel rather than a decelerating stream as originally intended.

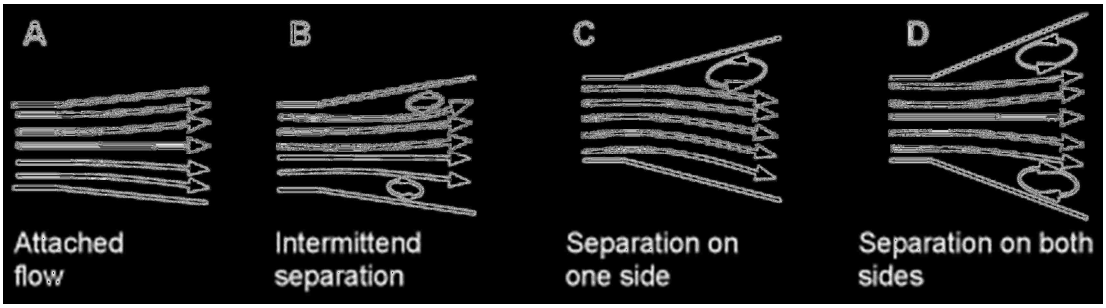


**Figure 6 – Four Regimes of Separation (Gülich, 2010)**

He also explains the negative effects of a thick boundary layer and that care must be taken with the upstream design to prevent them from forming despite an

adequate diffusor design. Figure 7 shows how a thick laminar boundary layer quickly decomposes to a much thinner layer with a turbulent regime.

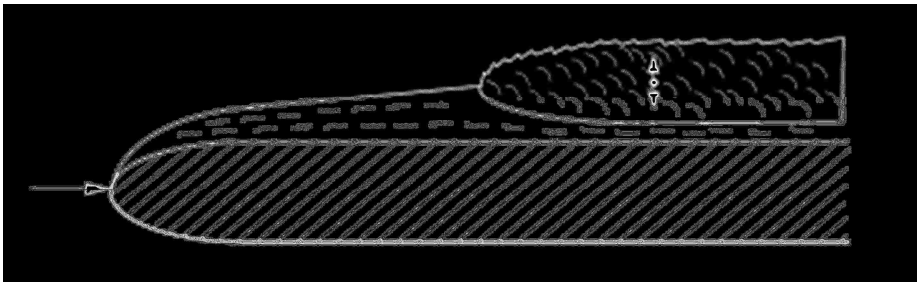

**Figure 7 - Laminar and Turbulent Boundary Layers (Gülich, 2010)**

Gülich specifically identifies upstream bends as a common cause of non-uniform velocity profiles (Gülich, 2010), which must be borne in mind because the diffusor passage is preceded by a spiral collector volute. This type of volute generates a non-uniform profile, known as a log profile, which is faster nearer the axis of rotation of the pump and decays logarithmically as it approaches the outer wall.

Flow through a bend always creates more hydraulic losses than a straight channel due to separation on the curved walls and secondary flows caused by the centripetal acceleration due to change in direction (White, 2003). The fluid traveling through the center of the bend is moving faster than that along the walls. This means that the particles in the center have a greater momentum than those along the walls, thus it is deflected to the outside of the path as it traverses the curved portion of the channel. Similarly, the flow traveling along the inside paths of the curve are subjected to greater acceleration because of the smaller radius of its path. This means that the inner particles are forced away from the bend by greater centripetal acceleration.

These two phenomena clearly set the stage for the classic counter-rotating twin spiral paths observed in planar curved passages. As the particles from the inner and center paths travel outwards due to momentum and acceleration, the particles along the outer paths are forced towards the inner paths of the bend via the boundary layer (i.e. the wall of the channel).

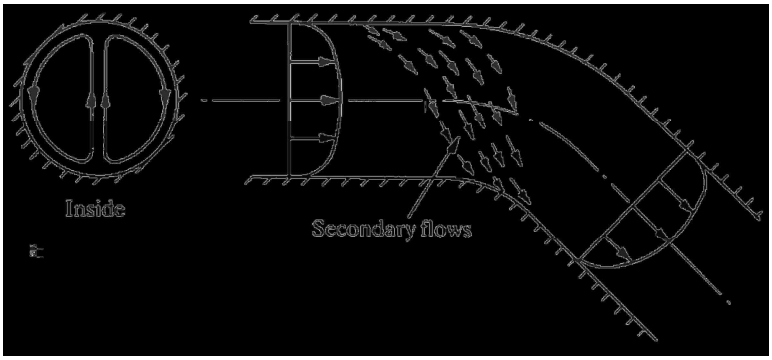


**Figure 8 - Secondary Flow in a Pipe Bend (Miller, 1990)**

The swirling flow pattern is very stable and requires between 50 to 70 diameters to resolve itself back into straight flow (Gülich, 2010). This swirling flow, in turn, experiences a longer flow path than straight flow would which results in higher friction losses and the existence of two extended vortex tubes dissipates energy out of the fluid. The extended length of the swirl is also problematic because the eye of the succeeding impeller is sensitive to approaching flow that is not tangentially uniform.

Another potential problem with the increased velocity due to the secondary flows is cavitation. Cavitation occurs when the local static pressure in a liquid flow field drops below the fluid's vapor pressure. At this point, the liquid will flash, that is

it will quickly vaporize. Further downstream, however, when the static pressure returns to a higher value, these bubbles of vapor will return to the liquid phase. When the vapor bubble collapses to the lower energy level of the liquid, the released energy causes a sudden localized pressure pulsation on the surface of the domain wall. This results in a lot of random noise and locally eroded areas in the walls. Miller identifies a cavitation parameter, $\sigma_b$, that relates the total pressure in a fluid to its vapor pressure and velocity as well as limits for this parameter in a pipe bend (Miller, 1990):

$$\sigma_b = \frac{H_{upstream} - H_{vapor}}{U^2/2g}$$

Where $H$ is the head, $U$ is the velocity, and $g$ is gravity.

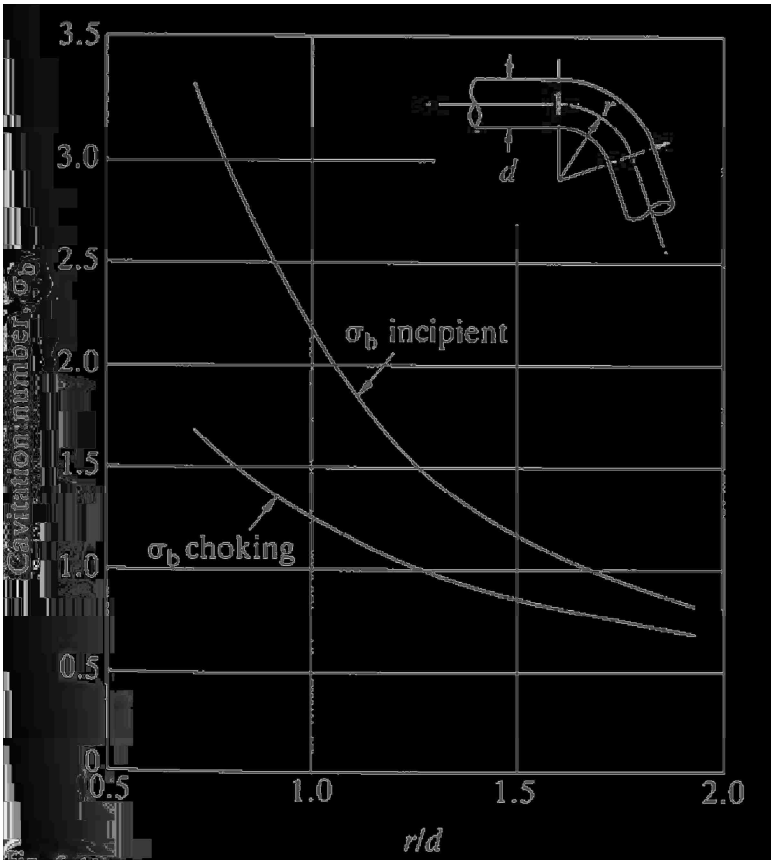


**Figure 9 - Cavitation Parameter for Bends (Miller, 1990)**

$\sigma_b$ can be used to analyze the crossover curvature for any locations that may be susceptible to cavitation damage and hydraulic losses. Cavitation is not expected to be a problem in the crossover because of the high total pressure entering the domain.

Miller also characterizes the interaction between bends and diffusors. In the case of the long crossover passage a diffusor is leading into a bend. This gives two design options. The first is to diffuse the flow, then bend it, the second is to bend and diffuse at the same time. In the first case, the diffusion should be concentrated towards the inside of the bend. This will give rise to some separation, but it will be

controlled and concentrated in one area at the end of the diffusor and just at the beginning of the bend (Miller, 1990).

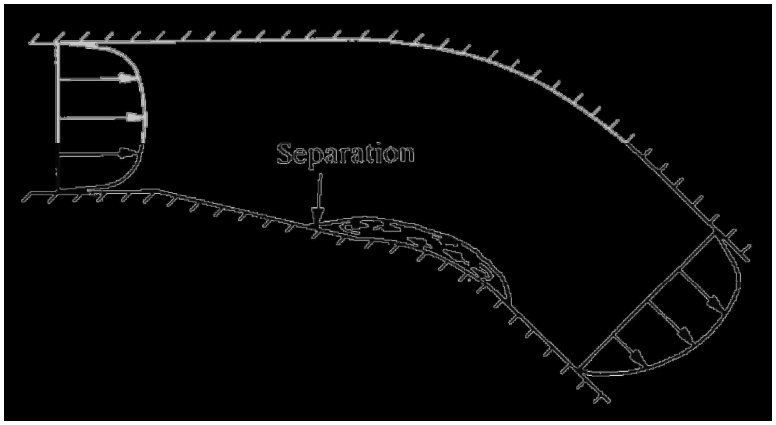


**Figure 10 - Diffusion into Bend (Miller, 1990)**

The second option can result in the least head loss, but the exit area to inlet area ratio has an upper limit of 1.5 and requires a parallel section after the diffusion to reconcile an area of slight mixing that develops along the inside of the bend (the same area where separation develops in the first option) (Miller, 1990).

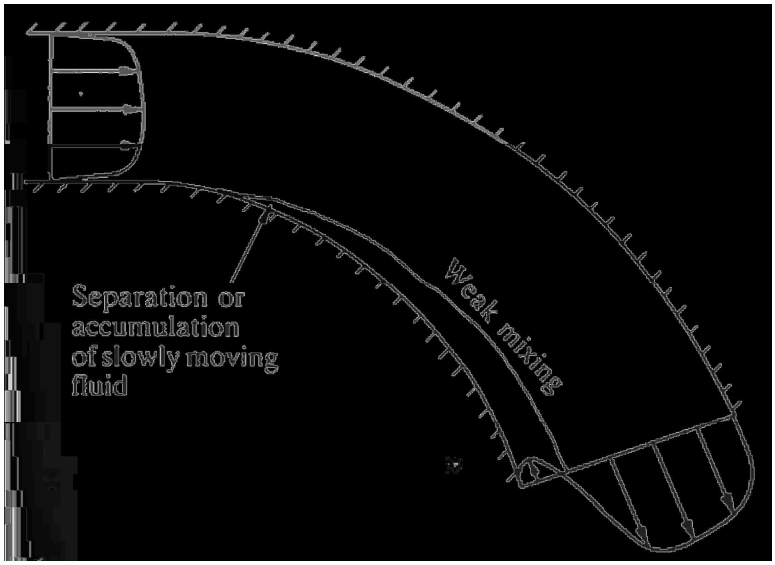


**Figure 11 - Continuous Diffusion and Bending (Miller, 1990)**

It should be noted in the illustrations above that the incoming flow is fully developed. In the case of the long crossover, the flow profile does not resemble this, but rather the inside of the bend has a velocity greater than that of the outside stream. It can thus be considered that the higher energy of the inside stream may keep it attached to the wall longer than demonstrated by Figure 10. If this turns out to be the case, then it may be possible to curve the flow path more aggressively because the flow can be expected to remain attached further along the crossover geometry.

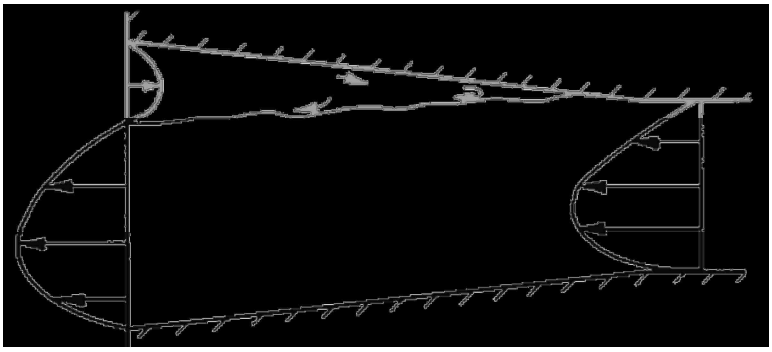

Figure 12 - Undeveloped Flow Entering a Diffusor (Miller, 1990)

A nozzle is the opposite of a diffusor; it converts potential (static pressure) energy into kinetic (velocity) energy. This energy conversion is a stable and low energy dissipation process (Miller, 1990). One primary difference, however, is the impinging flow has a high pressure at the wall that is being converted to a lower pressure (higher velocity). This means that rather than relying on viscous drag to keep the flow attached to the wall, the fluid's internal energy takes on this role. With a higher upstream pressure, the flow cannot separate from the wall and remains attached for the entire energy conversion process. This allows the flow to accelerate much more rapidly in the nozzle than the analogous deceleration in a diffusor. This results in a much shorter nozzle component relative to the diffusor component of the long crossover.

Another reason the nozzle is so important is that the rapid acceleration will redirect the flow down the center of the nozzle exit. This will have the tendency to straighten the streamlines from the double vortices that are entering the nozzle. This is extremely important to the performance of the pump because impeller inlet geometry

is fixed. If the flow is not axisymmetric entering the impeller eye, then the rotor/fluid interaction is not constant. Different interaction at different locations in the inlet can result in non-uniform pressure profiles along impeller inlet plane, giving rise to hydrodynamic forces and moments that may lead to rotor instability, vibrations, cavitation, and premature impeller failure.

# 2 Governing Equations & Numerical Procedure

In order to define the flow domain for this numerical analysis, a solid model has to be created. The governing equations must be defined and simplified, if possible, and the appropriate boundary conditions designated at the appropriate areas. Below is an explanation of the geometry creation and governing equations followed by the various analysis control parameters that were defined prior to executing the simulation.

## *2.1 Geometry*

The newly designed long crossover geometry is used as the fluid domain for this numerical simulation. This geometry was only provided as a two-dimensional layout, requiring its conversion to a three-dimensional solid model in a format that could be recognized by the CFD software package.

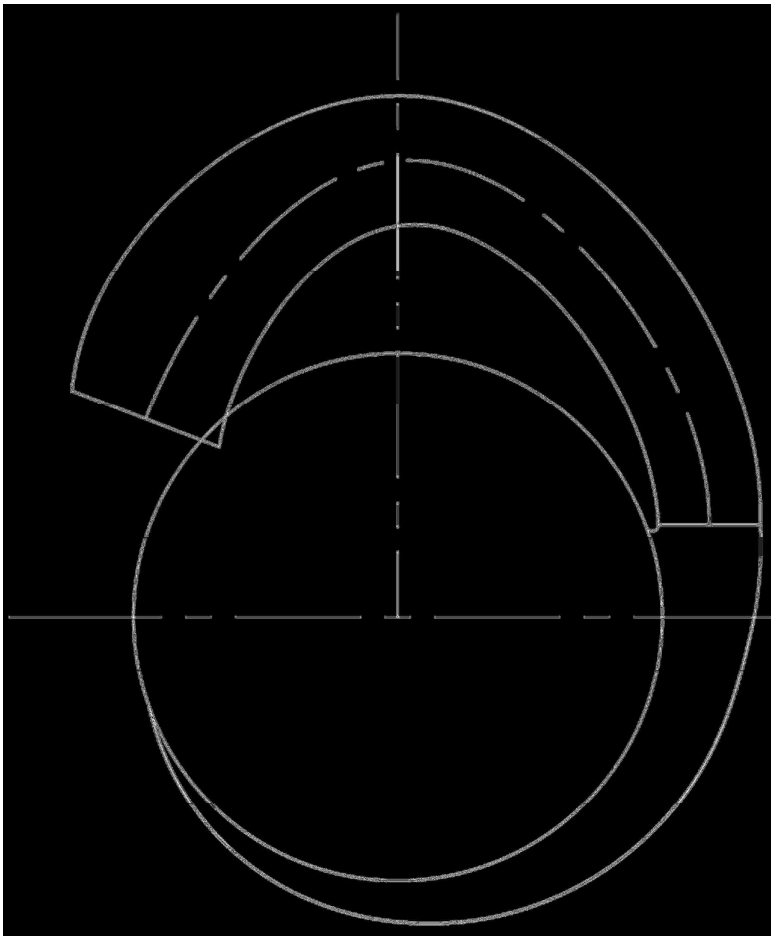

**Figure 13 – 2-D Side View of Crossover Geometry**

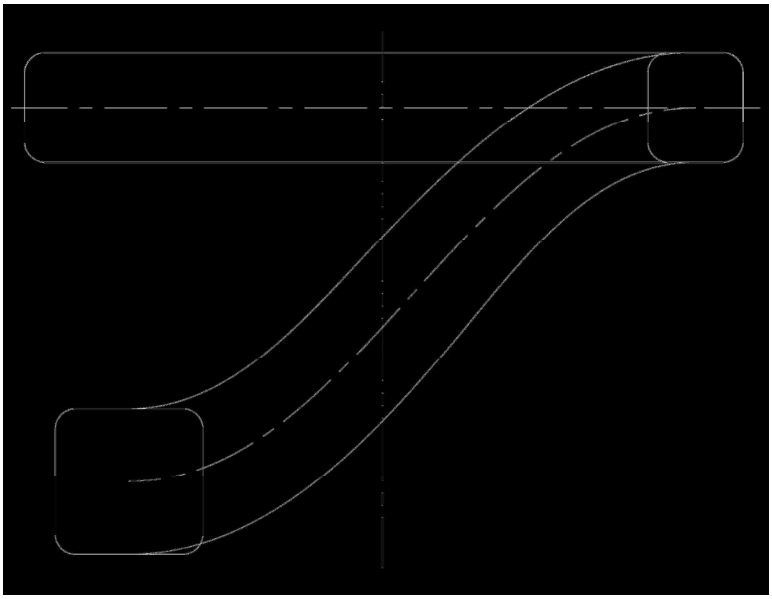

Figure 14 – 2-D Top View of Crossover Geometry

Using a commercially available solid modeling program and a commercially available drafting program, the geometry was painstakingly converted into a three-dimensional solid model.

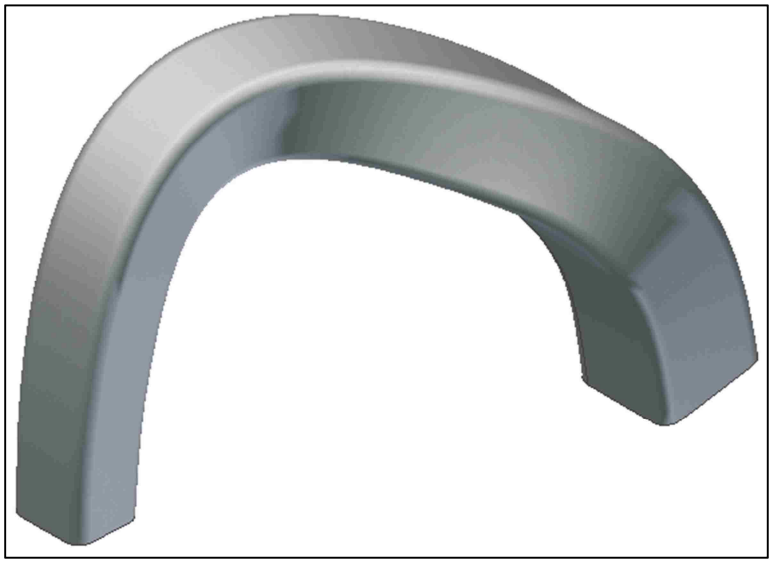

Figure 15 – Hydraulic Passage of Long Crossover (©Flowserve Corp. 2011)

Refer to Appendix A – Solid Modeling for a discussion of the importance of this relatively new capability and a detailed procedure for the creation of the long crossover solid model.

The data collection locations along the fluid stream were chosen by dividing the fluid domain into thirteen cross-sections. These include the inlet and outlet of the domain and eleven intermediate sections whose center points are radially spaced every ten degrees along the center line of the long crossover.

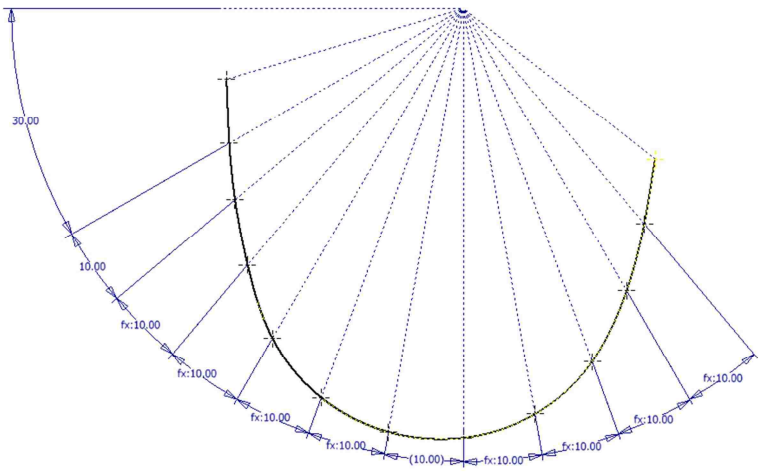


**Figure 16 - Cross-Section Locations (©Flowserve Corp., 2011)**

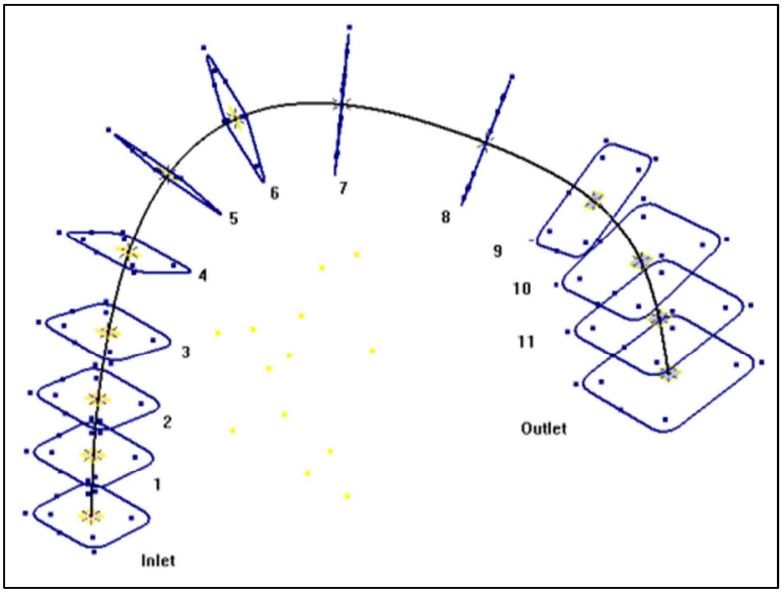


**Figure 17 - 3-D Cross-Sections with Labels**

It is known that the velocity profiles will not be uniform through the cross-sections, so the mass flow average[1] of the measured parameters will be determined along the mesh of each of these profiles.

## *2.2 Governing Equations*

Computational Fluid Dynamics (CFD), in its modern form, has been around for over thirty years. While great strides have been made in mesh generation, turbulence modeling, and other mathematical handling problems (e.g. singularities and stagnation points), the underlying theory remains the same; discretizing the governing fluid dynamics, heat and mass transfer, and other physical equations in a finite volume under given boundary conditions and solving them as efficiently as possible. For brevity, only the equations dealt with in this analysis are being listed.

The equations solved are the Navier-Stokes equations in their conservative form. The averaged mass and momentum conservation equations are discretized and solved along with the additional terms generated by the averaging process (see Appendix B – Turbulence Models for a discussion on generating the averaged terms and different models for handling the additional terms).

[1] $massFlowAve(\Phi) = \frac{\sum \dot{m}\Phi}{\sum \dot{m}}$, where $\Phi$ is variable being averaged and $\dot{m}$ is the mass flow rate (ANSYS, Inc., 2009)

These transport equations, in a stationary frame, can be written as follows:

- Conservation of Mass (Continuity)

$$\frac{\partial \rho}{\partial t} + \nabla \cdot \left(\rho \vec{U}\right) = 0$$

Where $\rho$ is the fluid density and $t$ is time.

- Conservation of Momentums

$$\rho\left(\frac{\partial \vec{U}}{\partial t} + \vec{U} \cdot \nabla \vec{U}\right) = -\nabla P + \nabla \cdot \tau + \vec{S}_M$$

Where $S_M$ is the body force vector, $P$ is static pressure, and $\tau$ is the stress tensor and relates to the strain rate by:

$$\tau = \mu\left(\nabla \vec{U} + \left(\nabla \vec{U}\right)^T - \frac{2}{3}\delta \nabla \cdot \vec{U}\right)$$

Where $\mu$ is the fluid dynamic viscosity and $\delta$ is the Kronecker delta.

In order to close these transport equations, the density function must be defined. This is necessary to ensure there are enough equations to solve for the number of unknowns in the analysis. This analysis is using incompressible water at a constant temperature, so the density is constant.

With this set of closed governing equations, the domain's boundary conditions must be defined. This is a straightforward analysis on a complex geometry. The boundary conditions have to be defined at the inlet, outlet, and along the walls of the

passage. The actual pump operating conditions (operating speed, flowrate, and head generation), however, are the end user's proprietary information and cannot be directly reported. The inlet of the flow domain was assigned the total pressure at the exit of the preceding stage and the outlet was assigned the mass flow rate. Finally, the passage wall was designated as a smooth, no-slip wall.

A subsonic inlet was defined at the opening with the smallest cross-sectional area. An inlet boundary will only allow flux in a single direction; into the fluid domain. The total pressure was designated with the direction for the incoming flow being normal to the opening.

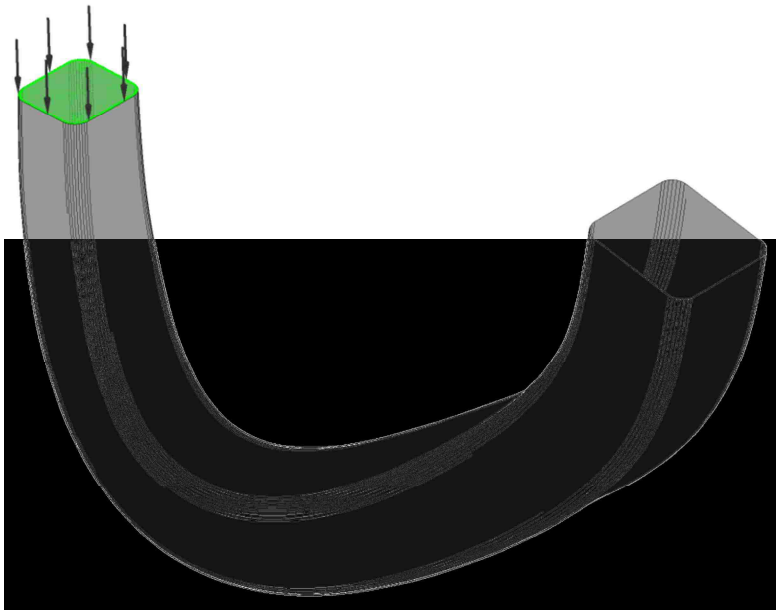

**Figure 18 - Location of Inlet Designation**

A subsonic outlet was defined at the opening with the largest cross-sectional area. An outlet boundary will only allow flux in a single direction; out of the fluid domain. The mass flow rate, $\dot{m}$, through the domain was designated at the opening. The mass flow rate is defined as:

$$\rho U = \frac{\dot{m}}{\iint dA}$$

Where $A$ is the area.

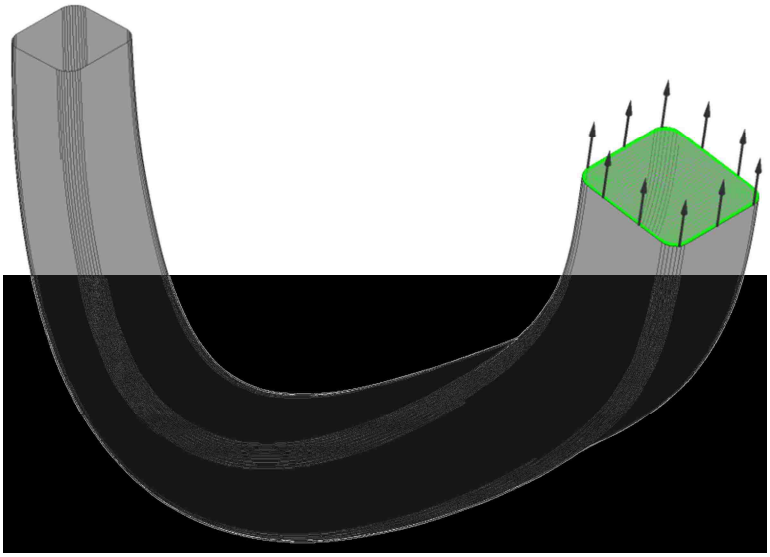

Figure 19 - Location of Outlet Designation

In this case, $\rho U$ is held constant for each surface integral on the inlet boundary face mesh. In this manner, the sum of all the area integrals will equal the total area of the boundary and the individual mass flow rate components will sum up to the total mass flow rate.

A wall is a rigid obstruction to the flow. Flow cannot cross the wall boundary, but it can have a significant effect on the flow field due to the tangential stress (shear) interactions. This is because of the classical no-slip velocity condition which sets the fluid velocity to zero at the wall, thereby inducing a non-uniform flow field. In an isothermal environment, the wall is considered adiabatic.

## *2.3 Meshing*

Meshing is an important part of any numeric simulation. The meshing process and the mesh resolution used both directly impact the simulation time and the simulation accuracy (as seen in Figure 23). While there are several methods available for meshing, only two were analyzed in this experiment. This is because the geometry being meshed is essentially a tube with a complex path and varying cross-section. The presence of a single clear inlet and single clear outlet, with no voids in between, lends itself wonderfully to the application of a swept mesh, which is the method that was eventually used.

A swept mesh divides a source face into surface elements, and then sweeps these surface elements to a target face using the geometry walls as guides. The lengths of the elements are manually dictated and should be chosen to maintain an aspect ratio of unity. Because the surface grid is similar on the source face and target face, the mesh is considered to be structured. A structured mesh follows a non-random (i.e. pre-defined) mesh element creation routine. A non-structured mesh uses an element creation algorithm to divide the volume into vertices obeying given sizing

and spacing parameters. These vertices are then connected to create a number of three-dimensional elements without guaranteed consistency in shape and size from one element to the adjacent ones.

Swept meshes can be free or forced. A forced mesh is one that uses a predefined face mapping. A free mesh is one that allows the meshing program to map the face using its internal generation engine. A forced mesh, then, can be conceptualized as a structured face grid, whereas a free mesh can be conceptualized as an unstructured face grid. The free mesh will account for curving surfaces and morph profiles from one contour to another. A free mesh was used for this simulation, although a forced mesh would have been acceptable due to the rectangular cross-sections being analyzed.

The primary parameter of interest is the head loss through the long crossover. Using this head loss as the basis for resolution, several different meshes were generated and simulated in order to identify the one with acceptable head loss convergence and minimal elements (i.e. simulation time). Table 1 lists the iteration results for several mesh sizes and different meshing methods.

Because the characteristics in the free stream were seen to be remaining approximately the same, the next modification was the inclusion of inflation. Inflation is the process of decreasing the normal spacing from the wall in order to make a series of successive elements that follow that wall's contour for a dedicated number of layers

with a dedicated growth rate. An inflated mesh is easy to identify by the dense layer of elements running parallel with the expected flow path.

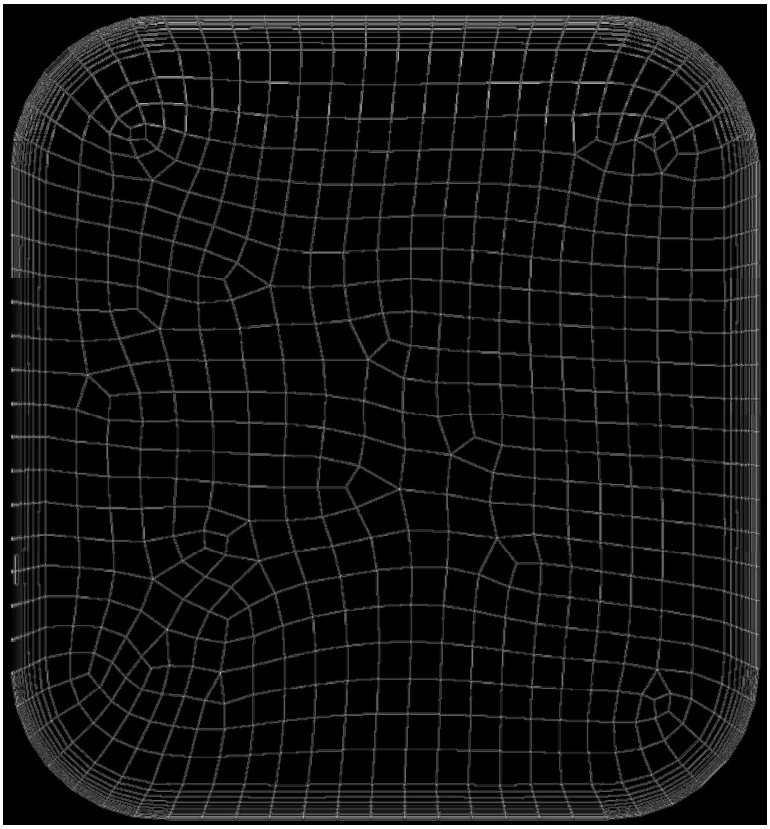

**Figure 20 - Example of an Inflated Mesh**

This inflation is important for resolving the velocity in the boundary layer near the walls. Different turbulence models exist for handling this flow region and these will be discussed later. The wall elements must be small enough to allow the free-stream velocity develop without premature conversion to the model specific wall function.

The second meshing method simulated was a free mapping tetrahedral method. In this method the three-dimensional geometry is randomly divided into tetrahedral

elements within defined size constraints by the meshing program. This method is computationally intensive on the front and back sides. It takes longer to generate the mesh and generates much more elements than the swept method does. This also leads to longer solve times because there are more elements to solve for.

### *2.4 Numerical Procedure*

The purpose of this analysis is to quantify the expected head loss in the crossover passage and identify areas that can be designed in such a way as to reduce this value. This being the case, the final evaluated variables are the change in head, ΔH, from the inlet geometry to the exit and the velocity and pressure profiles throughout the flow field.

The head loss in a CFD analysis is measured using the following equation:

$$\Delta H = \frac{P_{T,out} - P_{T,in}}{\rho g}$$

Total pressure, $P_T$, is defined as the pressure that would exist at a point if the fluid was brought instantaneously to rest (ANSYS, Inc., 2009). In an incompressible fluid, this becomes:

$$P_T = P_{Static} + \frac{1}{2}\rho\left(\vec{U} \cdot \vec{U}\right)$$

Although the net change from the inlet to outlet is of greatest interest, the fluid domain will also be monitored to identify areas with large total pressure gradients. These areas are of importance because they demonstrate where the greatest losses are

occurring. It is expected that the largest total pressure losses will occur in areas of high curvature because the changing direction should induce secondary flow patterns that dissipate velocity energy by their presence.

The flow profiles will be recorded at planar section cuts along the passage centerline. The plane locations will be at the intersection of radial planes with equal angular spacing and the plane orientations will be perpendicular to the three-dimensional centerline (see Figure 16).

The numerical simulations run for this pump are confined to the long crossover passage of the pump. Historically, past attempts to calculate hydraulic losses correlated to Reynolds number have never served a useful purpose. This is due to the prevalence of eddy losses caused by lack of streamlining and diffused flows in the impeller and casing. These eddy losses cause the skin friction losses associated with pipe flow analysis to become secondary losses (Stepanoff, 1993). However, because of the ease of storing and post-processing, Reynolds number will be monitored and reported at the cross-sections.

## *2.5 Simulation Setup*

### *Domain Definition*

A domain requires three specifications:

- One or more three-dimensional regions that constrain the fluid spatially
- The physical nature of the flow

- The material properties of the fluid

The bounding region is the solid model discussed in the Geometry section above. The crossover geometry was designated as a fluid domain and the reference coordinate system was made to coincide with the solid model's.

### *Fluid Properties*

In the case of the long crossover, the fluid was simply isothermal liquid water at 25ºC. This simplifies the analysis and reduces the computing time because there is no change in temperature (i.e. heat transfer) through the domain that needs to be simulated in the energy equation. If the pressure in the domain is predicted to drop below the vapor pressure of the water, then a cavitation model can be employed to analyze the effects of the phase change and pressure pulsations on the flow. Local pressures are not expected to reach such low levels, however, because of the large pressure present at the inlet boundary condition due to the energy addition of the first stage impeller.

### *Domain Model*

The crossover is a single stationary component and the fluid is isothermal, so there is no domain motion acting on the flow or density gradient to induce buoyancy. The potential energy change through the domain due to gravity is considered to be negligible when compared to the kinetic energy in the flow. With these assumptions, no buoyancy model, gravitational acceleration, or other external forces are activated for the simulation.

### *Fluid Models*

Just as the fluid domain must be modeled to account for any energy or momentum generated by externalities, the fluid itself must be modeled to define how the solver will handle complexities in the flow field. The fluid model definition activates the solver equations associated with different turbulence models, heat transfer, combustion, thermal radiation, and electromagnetics.

As mentioned above, the fluid is considered isothermal with no external energy or momentum sources for this simulation. This allows for all of the fluid model options to be turned off except for the turbulence.

Selecting a turbulence model is, quite possibly, the most important step in a fluid simulation. The turbulence model dictates how the non-linear components of the Navier-Stokes equations are handled and directly effects how secondary flows and boundary layers are treated in the solution. Appendix B – Turbulence Models contains a brief discussion on the advantages and disadvantages of the k-ε and SST turbulence models in ANSYS-CFX.

The mesh was refined using the k-ε model because it is less computationally expensive, then the more robust SST model was used to compare the differences in results (See Table 1).

## *2.6 Solver Controls*

To control the level of detail in the solver run, the resolution options for the advection and turbulence solving schemes must be defined. The advection term of the governing equations for a general variable, $\varphi$, is:

$$\nabla \cdot \rho \vec{U} \varphi$$

The discretization of this advection term results in higher order terms that make the solution more accurate, but also more computationally expensive. By limiting the solution to only looking at the first-order terms, the immediate "upwind" behavior can be simulated inexpensively with reduced accuracy. The same applies to the turbulence numerics. Flow separation is expected to occur in the curved passage, requiring increased accuracy both in the advection and turbulence solutions. The advection scheme was left at high resolution because the secondary flows are important. The turbulence numerics option was left at high resolution because the expected pressure gradients around the bends are expected to be adverse.

The length of the simulation is controlled by the minimum of the convergence of the momentum and mass flows or the maximum number of iterations. A simulation such as this one is expected to approach convergence between 50 and 100 iterations. Computer time was not an issue in running this simulation, so the iteration limit was set to 200 to ensure convergence. The convergence criterion was set to monitor the RMS residual of the mass flow and the directional components of the momentum. The documentation suggests a residual target of $10^{-5}$ for quantitative analysis, and that

is the value that was used (ANSYS, Inc., 2009). A mass conservation target of 1% was also designated, although it is probably unnecessary for such a simple flow domain.

Finally, the physical time scale was designated as .04s. In numerical solvers, the *relaxation method* is used to obtain numerical solutions to systems of equations. The time scale is a false timestep used by the ANSYS-CFX solver to under-relax the equations as they are iterated in order to speed up their convergence. Conceptually, the time scale is analogous to the constant, k, in an ordinary linear differential equation. The higher the k, the more "relaxed" the function will be and it approaches its asymptotic value faster. Similarly, if the time scale is large, the change in value from iteration to iteration changes faster and the solution converges quicker. The caveat here is that the solution has to converge smoothly, if not the larger iterative change in the solution can overshoot the converged solution and require another iteration to correct this. The numerical solution can then find itself in a situation where it constantly overshoots the solution and is constantly correcting itself. This can be seen in the residual monitor as an oscillating residual value. The lower the time scale, the more gradual the convergence, this leads to longer run times.

The general rule for selecting a time scale is to use the approximate amount of time a particle will spend in the fluid domain (ANSYS, Inc., 2009).

$$\Delta t \approx \frac{L}{U}$$

Where $L$ is the length of the mean pathline.

In the case of the crossover, this would be the length of the mean path line divided by the average velocity of the fluid. If the solution does not converge smoothly, reducing the time scale by a factor of four is a generally accepted way of checking the solution's sensitivity to this parameter.

# 3 Presentation and Discussion of Results

Several meshing iterations were analyzed to identify the proper combination of turbulence model, inflation layers, and element sizes. Convergence to the desired residual RMS value was achieved in the majority of the cases and a mesh was selected for the final analysis. Figure 21 demonstrates the convergence of the selected mesh.

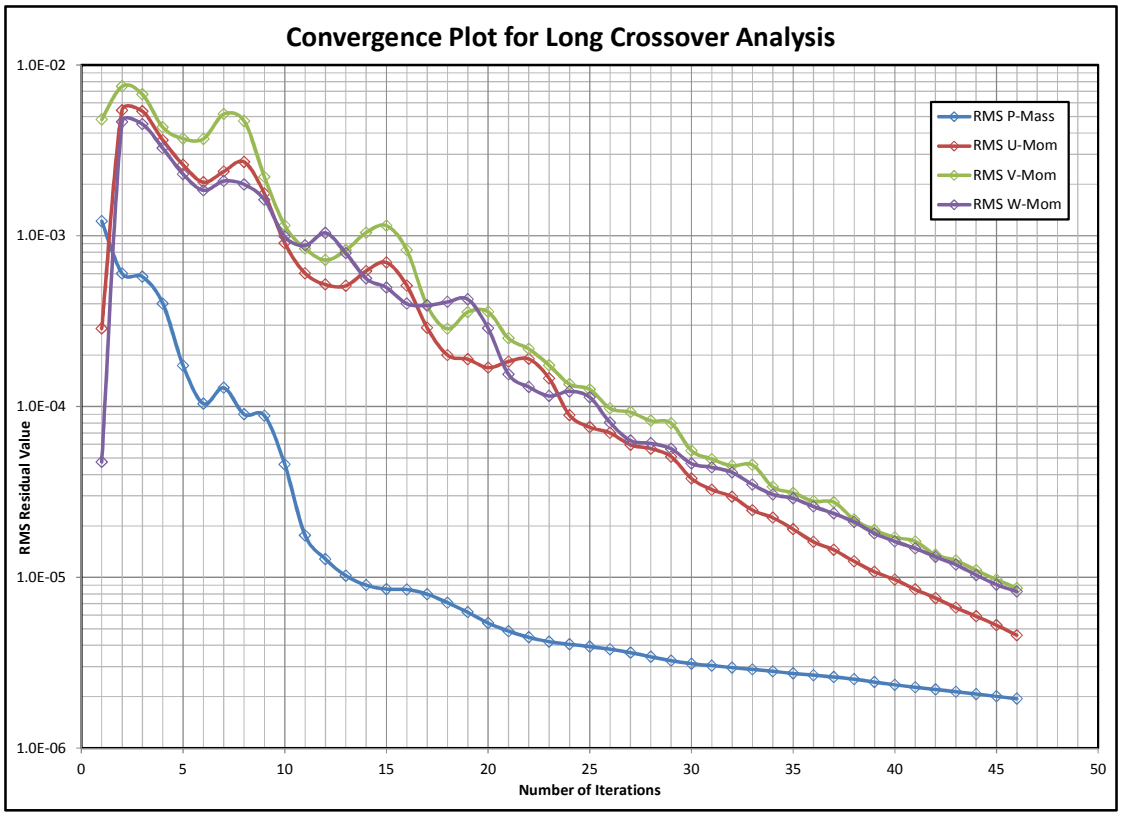


**Figure 21 - Convergence of Numerical Simulation**

Table 1 lists the different iterations and their resulting solve times and convergence.

Once the mesh was selected the results were processed. Beginning with a head loss analysis, the total pressure at each cross-section of the crossover will be plotted along the length of the mean path line. This total pressure will then be further separated into the velocity pressure and static pressure components to identify areas of high secondary flows. In a straight diffusor with no separation, the velocity pressure will decrease inversely with the area; if this expected pattern does not present itself, the section presenting the deviant values is immediately suspect as a candidate for

further study. The total pressure will be plotted at the cross-sections to compare the total pressure contours to the mean path line.

The velocity will be analyzed in the entire domain and at the designated cross-sections. The streamlines will be generated through the crossover and used to visually identify areas of separation and recirculation (if any). Velocity contours will be generated at the crossover cross-sections to show the magnitude of the secondary flows and domain area they occupy relative to the total area. The vectors will be mapped on the cross-sections to identify the locations of the secondary flow passing through each one.

The wall shear will be plotted along the crossover walls to identify areas of low shear. As outlined in the theory, the velocity of the fluid drops to near zero when separation begins to occur. By identifying the local areas with the lowest shear, it can be inferred that these are the areas where separation is impending.

## *3.1 Meshing*

| Mesh Refinement Iterations | | | | | | | | | | | |
|---|---|---|---|---|---|---|---|---|---|---|---|
| | | Mesh | | | | | Solver | | | | Notes |
| | | Method | Aspect Ratio | Inflation | Elements | Layers | Turbulence Model | Elapsed CPU Solve Time | Head Loss (in.) | Convergence | |
| I | 1 | Sweep | 1.78 | N | 20732 | N/A | k-e | 1.20E+02 | 150 | Y | 10X10 Elements on faces (.5 face spacing, .31 sweep spacing) |
| | 2 | Sweep | 1.35 | N | 108240 | N/A | k-e | 4.98E+02 | 149.3 | Y | 16X22 Elements on faces (.25 face spacing, .188 sweep spacing) |
| | 3 | Sweep | 1.42 | N | 788600 | N/A | k-e | 2.37E+03 | 139.3 | Y | 32X37 Elements on faces (.125 face spacing, .094 sweep spacing) |
| II | 4 | Sweep | N/A | Y | 44225 | 5 | k-e | 2.81E+02 | 168.4 | Y | .5 Total Inflation Layer Thickness |
| | 5 | Sweep | N/A | Y | 142205 | 5 | k-e | 5.77E+02 | 161.6 | Y | .25 Total Inflation Layer Thickness |
| | 6 | Sweep | N/A | Y | 787955 | 5 | k-e | 2.58E+03 | 148.9 | Y | .125 Total Inflation Layer Thickness |
| III | 7 | Sweep | N/A | Y | 77855 | 10 | k-e | 2.79E+02 | 163.9 | Y | .5 Total Inflation Layer Thickness |
| | 8 | Sweep | N/A | Y | 222508 | 10 | k-e | 8.38E+02 | 157.9 | Y | .25 Total Inflation Layer Thickness |
| | 8A | Sweep | N/A | Y | 486433 | 10 | k-e | 1.31E+03 | 151 | Y | .1875 Total Inflation Layer Thickness (.1875 face spacing, .125 sweep spacing) |
| | 8B | Sweep | N/A | Y | 488628 | 10 | k-e | 2.73E+03 | 152.5 | Y | .0825 Total Inflation Layer Thickness (Same spacing as 8A) |
| | 9 | Sweep | N/A | Y | 1095473 | 10 | k-e | 3.56E+03 | 146.7 | Y | .125 Total Inflation Layer Thickness |
| | 9A | Sweep | N/A | Y | 5883686 | 10 | k-e | 3.58E+04 | 148.8 | Y | .0825 Total Inflation Layer Thickness (.0825 face spacing, .05 sweep spacing) |
| IV | 10 | Sweep | N/A | Y | 1049489 | 10 | SST | 4.81E+03 | 137.9 | Y | .25 Total Inflation Layer Thickness (.125 face spacing, .094 sweep spacing) |
| | 11 | Sweep | N/A | Y | 1095473 | 10 | SST | 5.78E+03 | 145.2 | Y | .125 Total Inflation Layer Thickness (.125 face spacing, .094 sweep spacing) |
| | 12 | Sweep | N/A | Y | 1110801 | 10 | SST | 6.04E+03 | 149.8 | Y | .0825 Total Inflation Layer Thickness (.125 face spacing, .094 sweep spacing) |
| V | 13 | Tetrahedron | 1.73 | N | 818093 | N/A | k-e | 2.84E+03 | 142.5 | Y | .5 mesh sizing, .31 max element size, .031 min |
| | 14 | Tetrahedron | 1.8 | N | 2878145 | N/A | k-e | 1.10E+04 | 141.9 | Y | .25 mesh sizing, .188 max element size, .0188 min (Convergence >100 iterations) |
| | 15 | Tetrahedron | 1.58 | N | 23339756 | N/A | k-e | 5.89E+04 | 161 | N* | .125 mesh sizing, .094 max element size, .0094 min *Eventually would have converged |

**Table 1 - Mesh Refinement**

The initial swept mesh for this simulation, Mesh I, was sized such that there were approximately ten elements across the inlet face. The idea was that this would be enough to adequately resolve the velocity profile. Past experience has shown that this geometry requires a number of elements on the order of $10^6$, so the low number of elements generated by this coarse mesh immediately warranted skepticism. The mesh took approximately fifteen seconds to converge, which is also a warning sign. The following two iterations simply decreased the surface spacing and the element sweep lengths by half and the number of elements increased accordingly. The head loss also changed enough to continue reducing the spacing.

Mesh II and Mesh III used five and ten inflation layers, respectively. The total thickness spanned by the layers coincided with the face spacing; this means that the inflation layers were fully contained within the area that would have been the first element building off the wall. After being simulated, the velocity distribution along the outlet was visually inspected to determine whether the behavior at the wall was acceptable. It was seen to behave better with ten layers rather than five. This makes sense because it gives the flow more spatial resolution in which to slow down as it approaches the wall. The elements directly adjacent to the wall contain the turbulence model wall blending function and this is easily observed by the quickly decreasing velocity in this element.

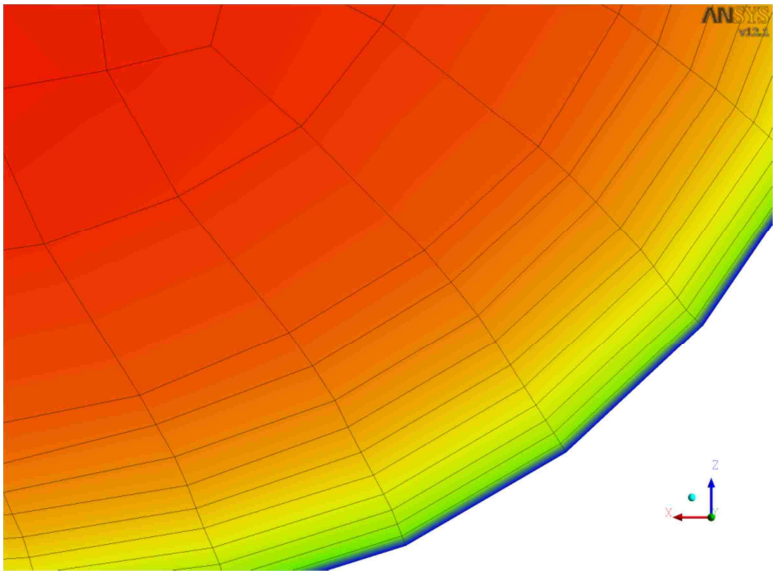

Figure 22 - Velocity Behavior Near the Wall

The velocity is slowing down as expected and the deceleration increases as it approaches the wall. The changing velocity does a good job of smoothly transitioning from the free-stream velocity to zero throughout the inflation layers and this is considered an adequate number of layers for this simulation.

As expected, the number of elements generated for Mesh IV was orders of magnitude greater than that of a swept mesh, driving the solve time up an order of magnitude as well. This method also converged more slowly, taking both more time per iteration and more iterations to converge. This is because the swept mesh is much more uniform in element shape and size, so it lends itself to quicker, more efficient solving.

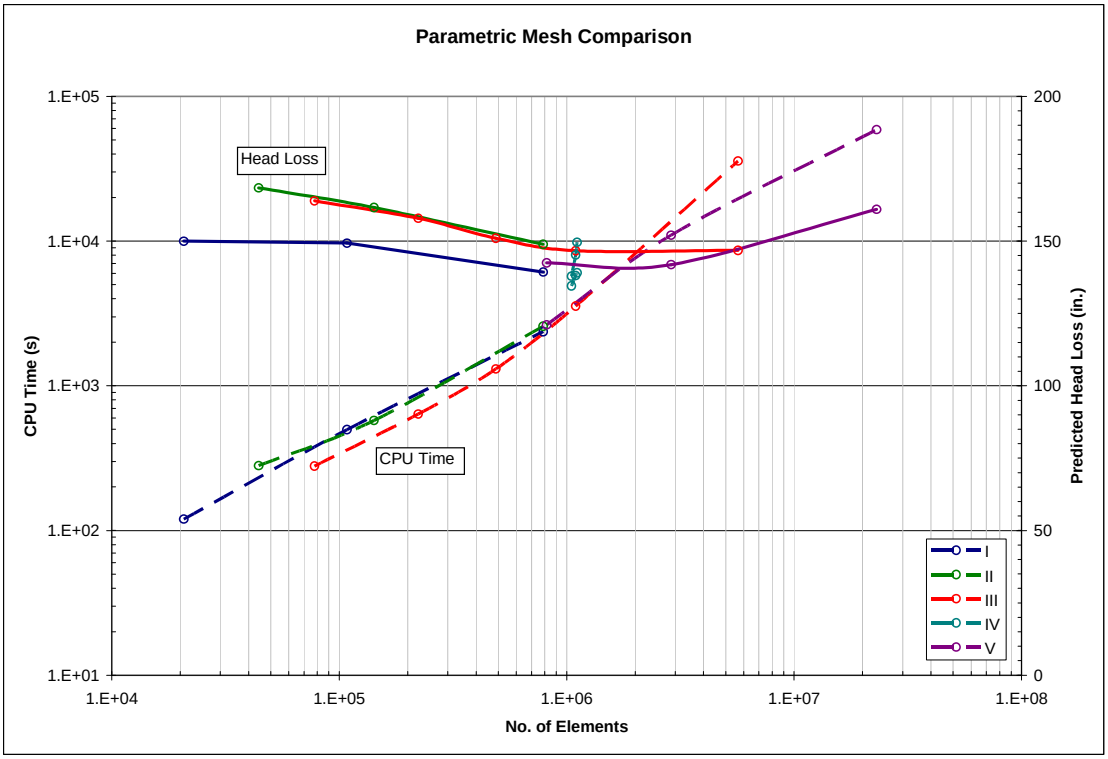


**Figure 23 - Time and Head Loss vs. Number of Elements**

Figure 23 plots the CPU time (dashed lines) and head loss (solid lines) versus the number of elements for each arrangement. In the Mesh III arrangements it is seen that a five-fold increase in elements from Mesh III-9 to Mesh III-9A results in a ten-fold increase in CPU time for only a .1" change in head loss (<.1%). It should also be noted that the head loss for Mesh V seems to increase rapidly for its highest number of elements. This is due to the fact that this run did not converge fully. It was showing signs of convergence, but the amount of time required to fully converge would have been prohibitive to using this mesh anyway.

The difference in head loss value was seen to be approximately three feet. This equates to about a 1.2% difference between the two turbulence models. This is

considered small enough to justify using the faster k-ε model and the reported results were generated with this turbulence model.

In the end, Mesh III-9 was chosen as the appropriate arrangement.

### *3.2 Pressure*

The total pressure and its components showed smooth transitions from their original values at the inlet to their final values at the outlet. The total pressure at the inlet was used to normalize all of the pressure values and the length of the mean path line was used to normalize the cross-sectional locations from the inlet to the outlet.

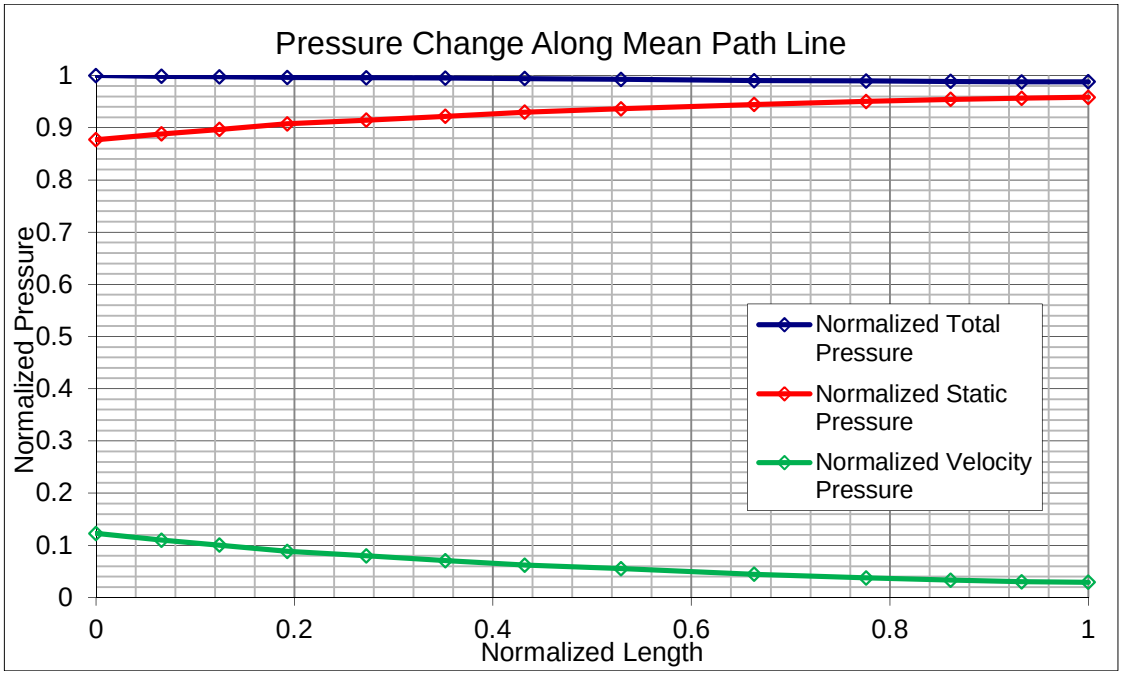


**Figure 24 - Pressure Loss Through Crossover**

The total pressure drops only 1.2% from inlet to outlet, meaning that the hydraulic efficiency for the long crossover is 98.8%. This is a very high efficiency

and the chances for improving upon it are relatively small. A great deal of effort will have to be spent in order to pick up a few tenths of a percent of efficiency. The expected causes of the losses are the secondary flows developed in the bends and the increased friction losses associated these higher local fluid velocities.

The velocity pressure begins by decreasing and levels out as expected towards the outlet. Taking the calculated average velocity at each cross-section and plotting them alongside the simulated average values shows close agreement between the analytical and numerical values. Again, the pressure value was normalized to the total pressure at the inlet. This trend in the velocity pressure data implies that the losses are occurring due to the frictional effects of the passage and separation more so than wasted energy in the secondary flows. This finding is counter-intuitive because, as stated above, it is expected that the losses in a 180º turn be dominated by secondary flows.

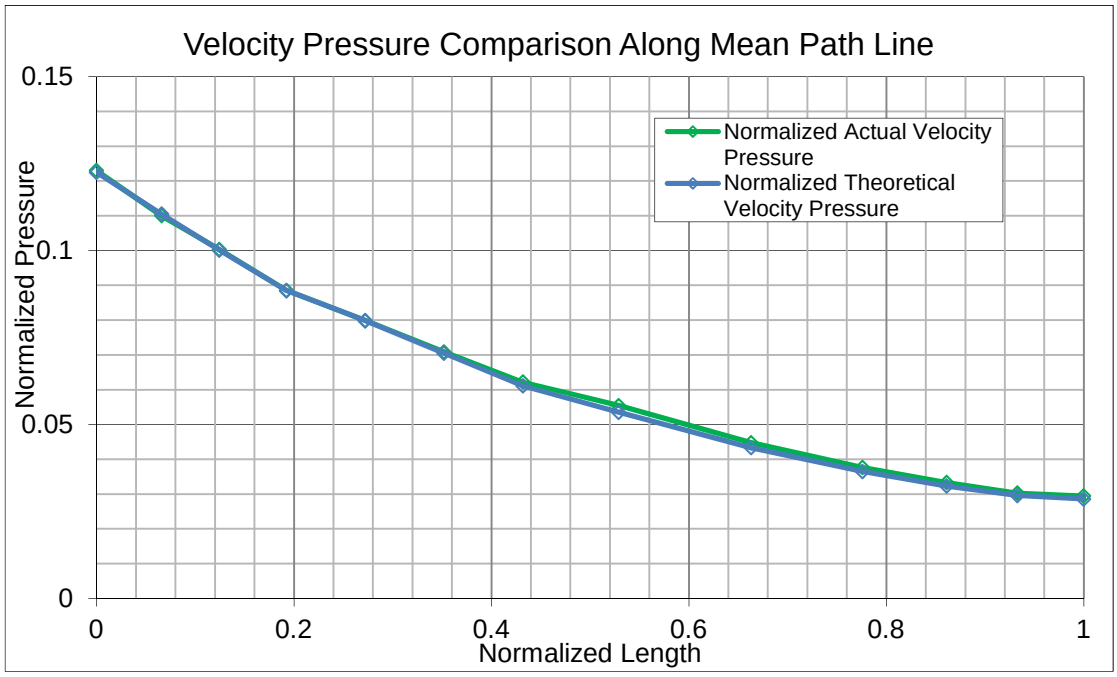


**Figure 25 - Velocity Pressure Comparison**

The static pressure begins by increasing linearly, and then it starts to level out. This can be interpreted as the diffusion process beginning to take place as expected, but then the process is interrupted. Subtracting the simulated velocity pressure from one (the normalized total pressure at the inlet) yields the theoretical static pressure given complete conversion from velocity to static pressure. This theoretical static pressure is plotted alongside the simulated static pressure for comparison. The simulation data begins diverging from the theoretical value immediately. The difference between the two values continuously increases until the ninth cross-section, where the difference levels out. This cross-section is where the passage begins to straighten out again to dump into the eye of the next impeller. This agrees with the expected result of the losses occurring in the bend, although not for the expected reason.

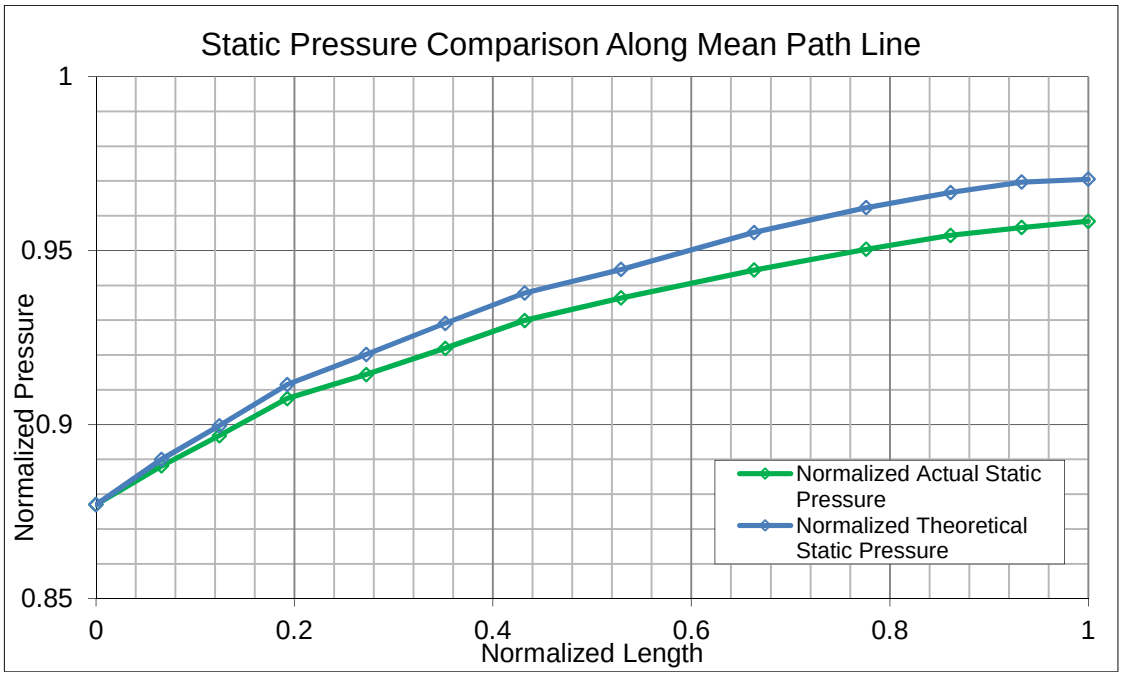


**Figure 26 - Static Pressure Comparison**

This loss is most likely caused by separation due to the emergence of secondary flows within the passage. As the secondary flows begin to develop, the flow cannot diffuse in its most efficient manner. The flow in the crossover begins to resemble regimes C and D in Figure 6. The expected vortex tubes travel through a smaller area than the desired developed flow front would. This means that the passage does not convert the velocity pressure into static pressure, but rather dissipates this energy in the separated regimes lining the vortex tube.

The crossover bends across the body of the pump in one continuous axial bend and two oppositely curving transverse bends. This indicates that the secondary flows should begin developing along the inside of the passage (in the +y direction according to the coordinate system in Figure 27) and axially away from the inlet and outlet (in

the -z direction according to the coordinate system in Figure 28). The flow should remain at the inside of the passage because there is no inflection in the axial direction, but it should change sides transversely due to the inflection in the transverse path of the crossover meanline.

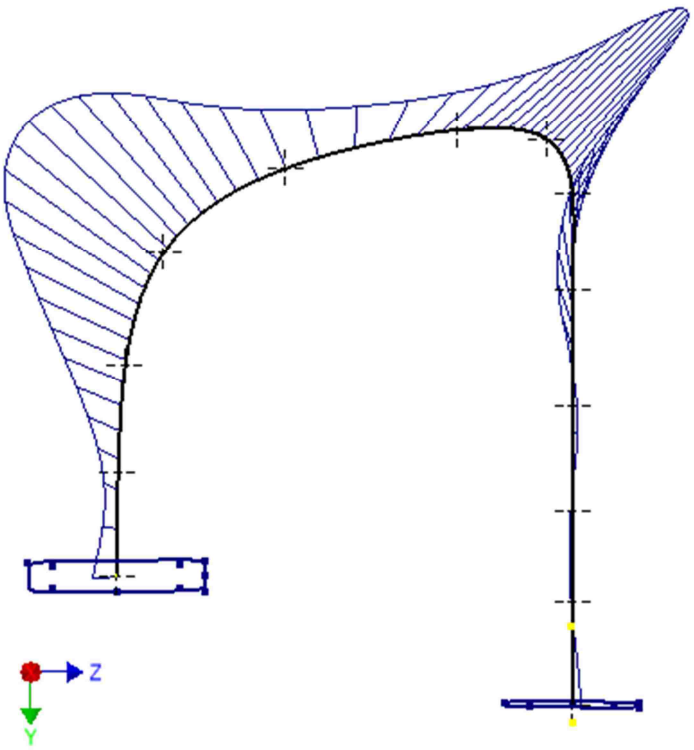


Figure 27 - Crossover Meanline Curvature - Side View

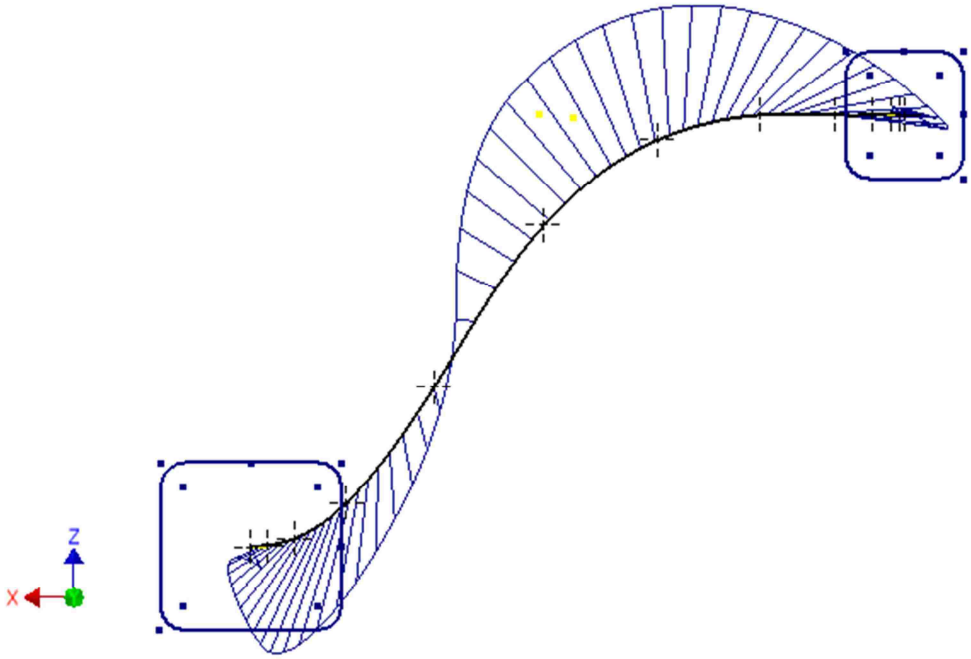


Figure 28 - Crossover Meanline Curvature - Top View

As expected the secondary flow develops at the inner surface of the passage due to the continuous curvature. The pressure contours at the cross-sections show where the secondary flows are developing. Beginning at the inlet and proceeding through the first five cross-sections, the flow is developing in the crossover. Beginning at the sixth cross-section and proceeding through the eighth cross-section, the secondary flow is developing in the inner left corner of the passage and beginning to shed off the wall. The ninth through eleventh cross-sections and the outlet show the vortex tube crossing along the inner path of the cross-sections and beginning to impinge upon the right wall.

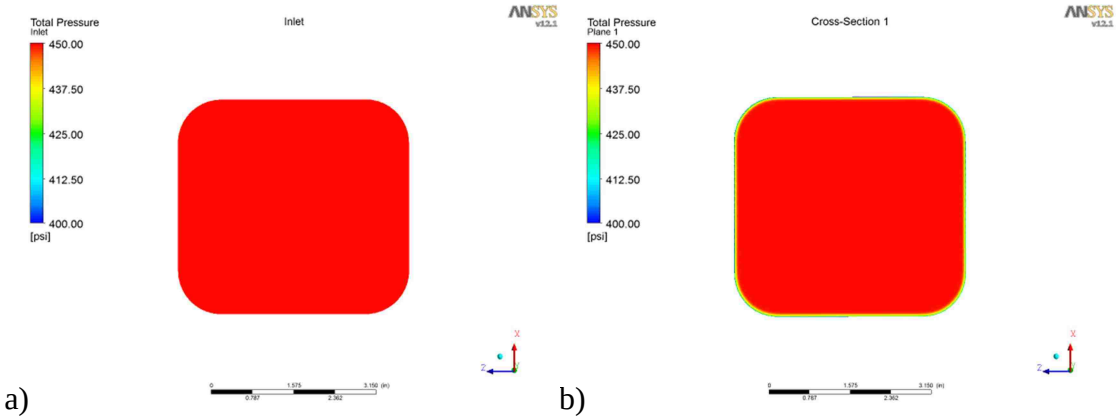
Total Pressure
Inlet
450.00
437.50
425.00
412.50
400.00
[psi]
Inlet
ANSYS
v12.1

a)


Total Pressure
Plane 1
450.00
437.50
425.00
412.50
400.00
[psi]
Cross-Section 1
ANSYS
v12.1

b)

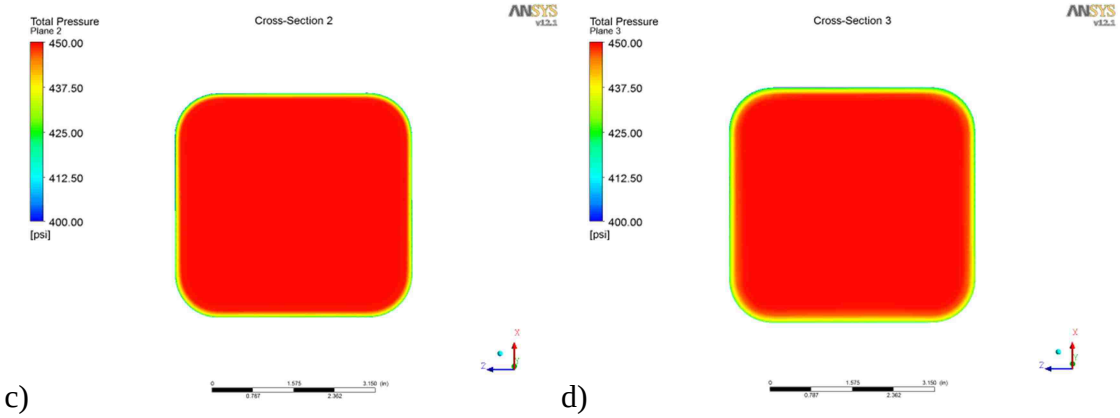
Total Pressure
Plane 2
450.00
437.50
425.00
412.50
400.00
[psi]
Cross-Section 2
ANSYS
v12.1

c)


Total Pressure
Plane 3
450.00
437.50
425.00
412.50
400.00
[psi]
Cross-Section 3
ANSYS
v12.1

d)

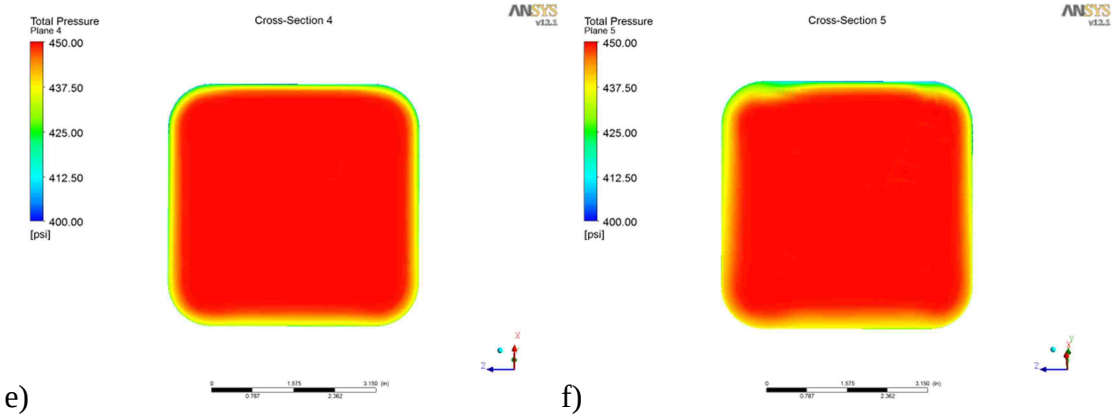
Total Pressure
Plane 4
450.00
437.50
425.00
412.50
400.00
[psi]
Cross-Section 4
ANSYS
v12.1

e)


Total Pressure
Plane 5
450.00
437.50
425.00
412.50
400.00
[psi]
Cross-Section 5
ANSYS
v12.1

f)

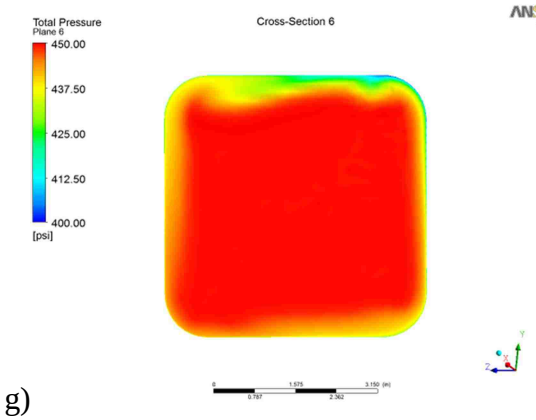
Total Pressure
Plane 6
450.00
437.50
425.00
412.50
400.00
[psi]
Cross-Section 6

g)

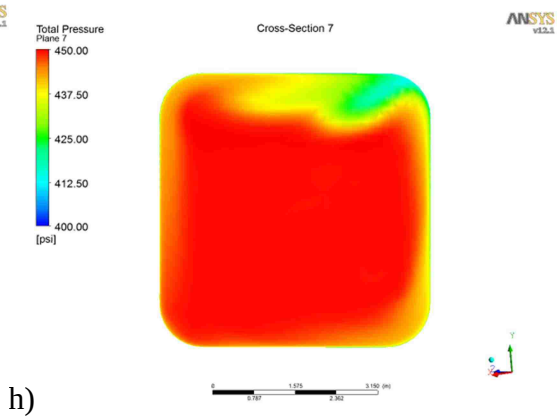
Total Pressure
Plane 7
450.00
437.50
425.00
412.50
400.00
[psi]
Cross-Section 7

h)

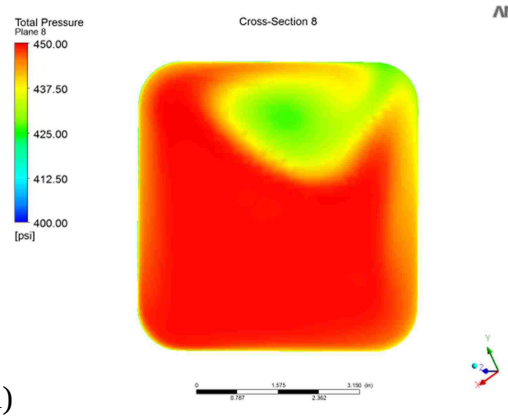
Total Pressure
Plane 8
450.00
437.50
425.00
412.50
400.00
[psi]
Cross-Section 8

i)

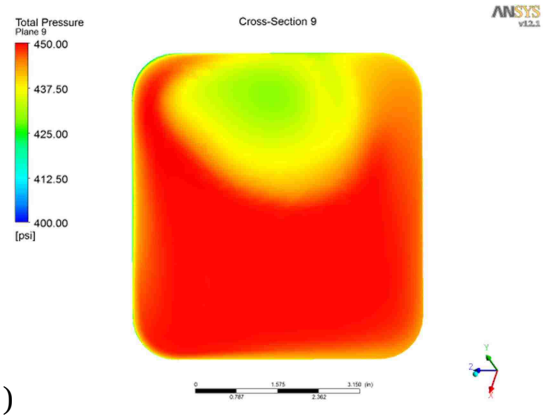
Total Pressure
Plane 9
450.00
437.50
425.00
412.50
400.00
[psi]
Cross-Section 9

j)

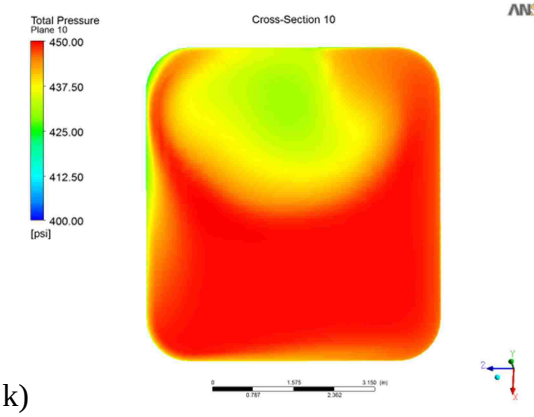
Total Pressure
Plane 10
450.00
437.50
425.00
412.50
400.00
[psi]
Cross-Section 10

k)

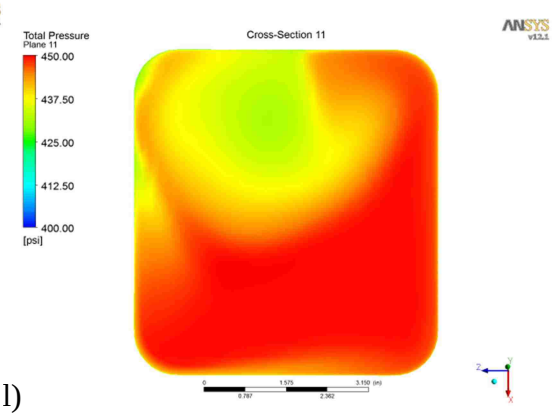
Total Pressure
Plane 11
450.00
437.50
425.00
412.50
400.00
[psi]
Cross-Section 11

l)

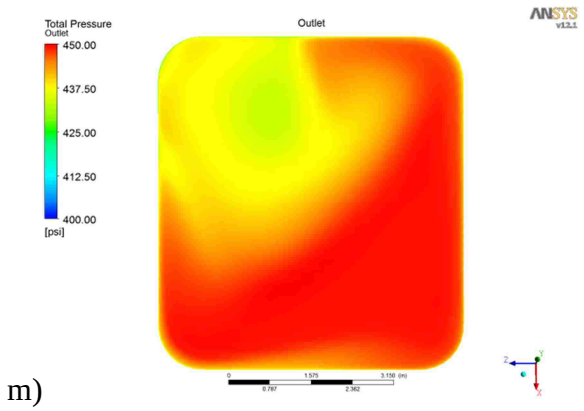


m)

**Figure 29 (a-m) - Cross-Sectional Total Pressure Profiles from Inlet to Outlet**

The pressure was also used to determine the cavitation number along the mean path line. Figure 9 shows an incipient value of approximately 3.5, the crossover has a minimum value of 8. The minimum is at the inlet, where it is demonstrated that the pressure profiles are relatively uniform. The real gradients do not appear until the seventh cross-section, which corresponds to about .53 along the normalized length. At this distance the cavitation number is approximately 17, well above the minimum threshold value of 3.5. It can therefore be stated with confidence that the flow is not cavitating anywhere along the passage walls in the domain.

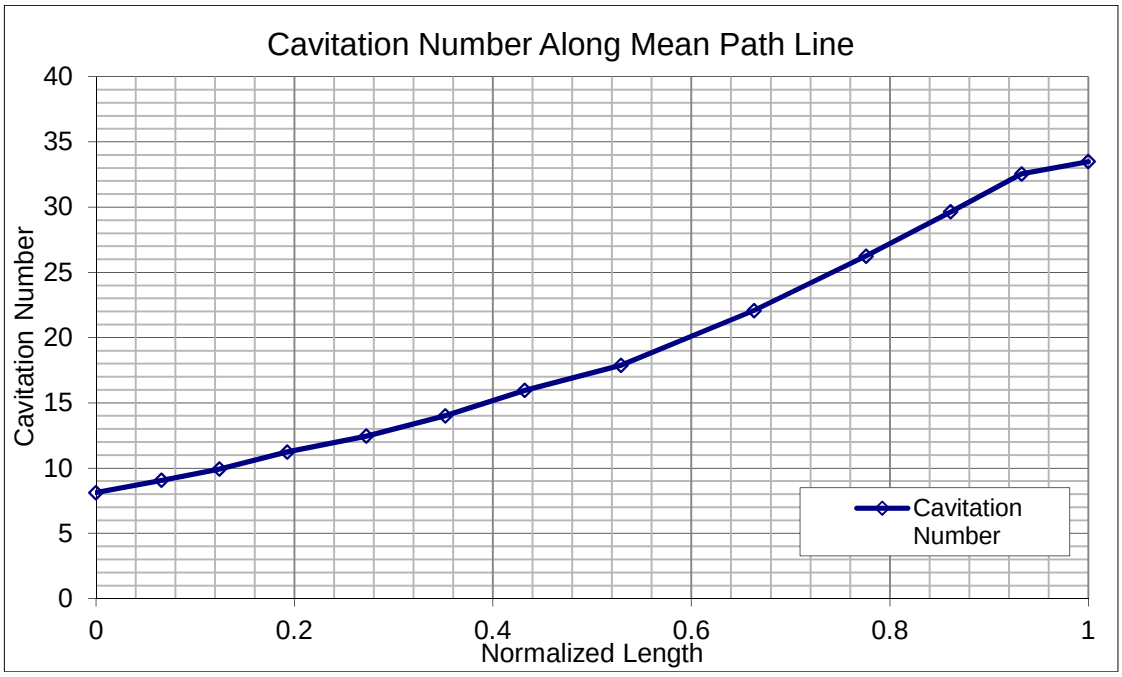


**Figure 30 - Cavitation Number along the Normalized Length**

## *3.3 Velocity*

An analysis of the Reynolds Number through the crossover shows that the flow falls into the transition zone from laminar to turbulent flow. Plotting the Reynolds Number and relative roughness on a Darcy-Weisbach chart shows very little change in friction factor in the Reynolds Number range of the flow. However, this information is not enough to estimate the head loss in the domain because of the presence of secondary flows.

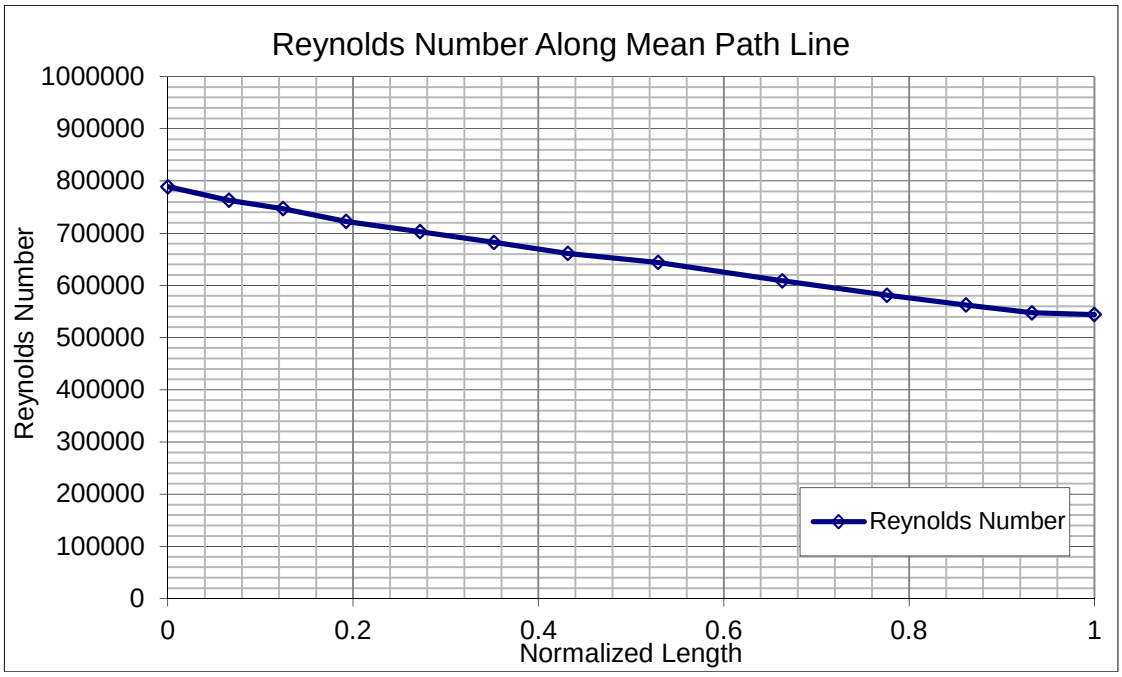


**Figure 31 - Reynolds Number along Mean Path Line**

The first through sixth sections show evidence of the flow profile distorting to favor the outer wall. This is to be expected in a planar bend; the secondary flows will not be evident until the flow is at the end of the first curved passage. The secondary flow begins to develop around the seventh section and is still present at the outlet. The seventh section is at the downstream end of the first complex bend (that is where the bending occurs in two planes). The development of the secondary flow is accelerated by the new bending direction. By the time the ninth section is reached, the swirling flow is well-developed. This flow is carried out of the crossover and introduced to the suction passage of the succeeding impeller eye.

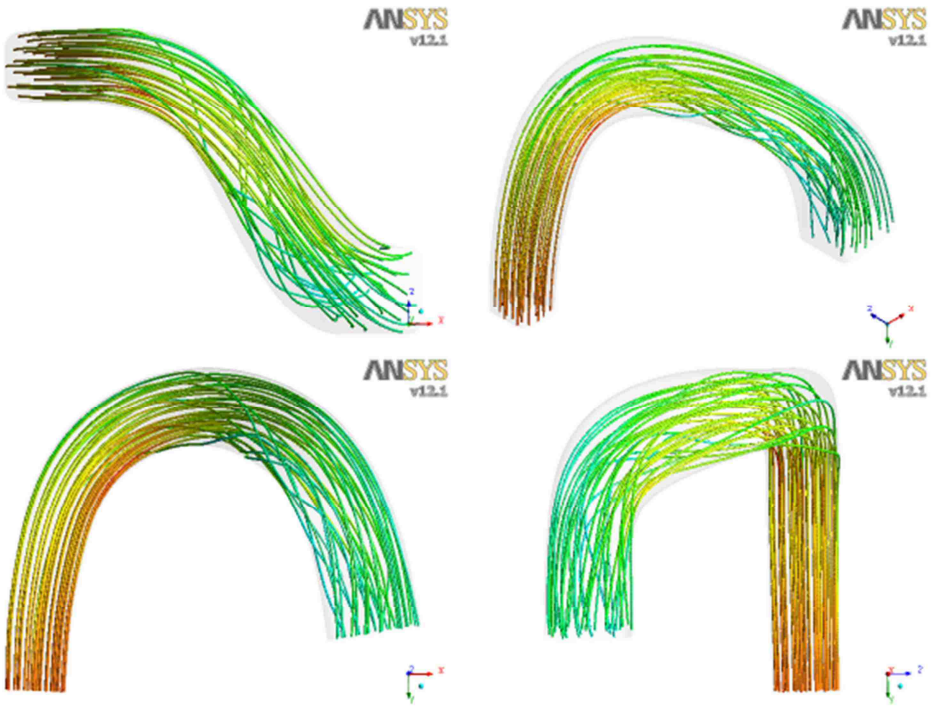


Figure 32 - Streamlines Through Crossover

Closer inspection of the seventh through ninth cross-sections shows the streamlines swirling through the low total pressure areas in the cross-section. This visualization demonstrates that although the secondary flows are present, they do not cause a large change in the velocity of the stream (i.e. the meanline off-axis components are small compared to the meanline axial direction). This low energy difference between the free-stream and simulated velocity fields may account for the negligible difference between the theoretical and simulated values for the velocity pressure. With this knowledge, it may be possible to control where the secondary flows are developed because their presence does not seem to be a problem compared to separation losses.

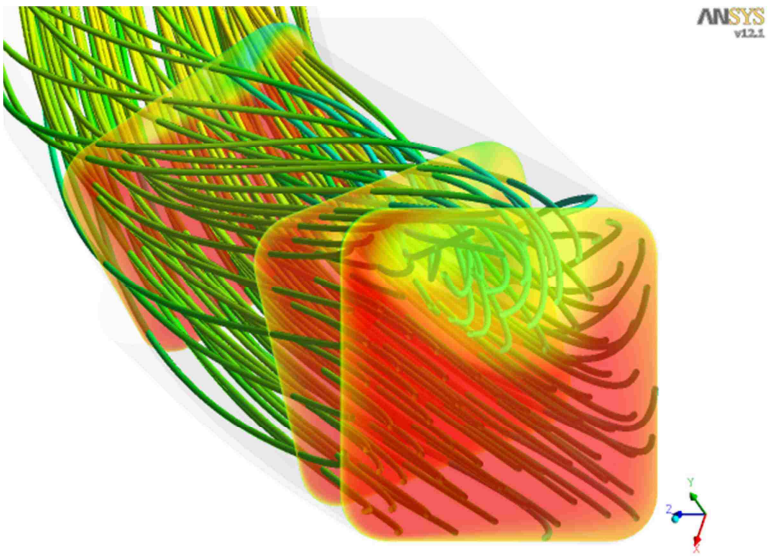


Figure 33 - Development of Secondary Flow Pattern

The vortex tube then migrates to the other corner of the passage as the crossover performs its final complex bend before emptying into the suction of the next stage. This portion of the flow is very important because it determines the behavior of the flow field entering the eye of the succeeding impeller. As mentioned before, the incoming flow must be as tangentially uniform as possible in order to minimize the variation in the angle of attack at the impeller blade. The more swirling present in the vortex tube, the harder this is to achieve. This means that although the velocity pressure losses are minimal, the downstream effects may be considerable and it may be prudent to develop an approach geometry that cleans them out of the flow via an acceleration process.

The cross-section velocity contour plots are seen to corroborate the trends in the cross-section pressure profiles. There is strange behavior at the fourth and fifth cross-sections where the fluid speeds up in the corner, only to slow down and migrate

across the inner path of the passage with the vortex tube. This behavior is seen to parallel the information in the pressure contours.

These cross-sections are at the beginning of curvature in the first transverse bend. Knowing that the preceding velocity profile is free of secondary flows, this begins to make sense. The curvature introduced upon the developed flow is the cause of the secondary flows. These two areas of fast localized velocities are the beginnings of the vortex tube that then propagates through the rest of the passage, actually causing a region of slow localized velocities downstream.

Also evident in the seventh and eighth cross-sections are small regions of stagnation in the corner of the inner path of the passage. This is indicative of flow separation and occurs just downstream of the high velocity stream. This is in agreement with experimentally observed flow separations as outlined in the literature from the Introduction. **This evidence of separation would be the root cause of the total pressure loss in the long crossover**. These regions are quite small, however, which also trends with the observed simulated data. There is only a 1.2% reduction in total pressure from the inlet to the outlet, meaning that any losses due to separation would have to occur in a very small area.


Velocity
Inlet
100.00
75.00
50.00
25.00
0.00
[ft s^-1]
Inlet
ANSYS
v12.1

a)

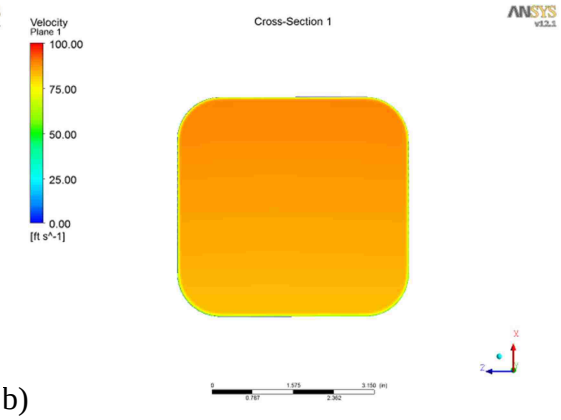
Velocity
Plane 1
100.00
75.00
50.00
25.00
0.00
[ft s^-1]
Cross-Section 1
ANSYS
v12.1

b)

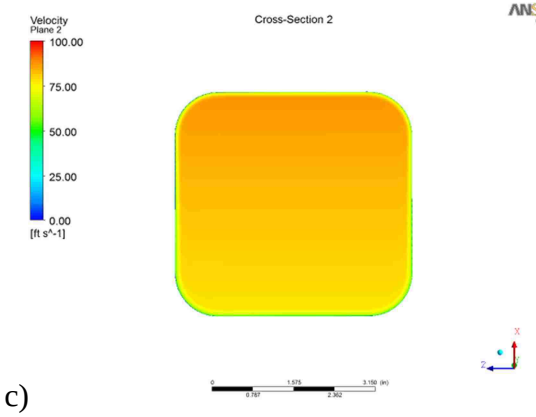
Velocity
Plane 2
100.00
75.00
50.00
25.00
0.00
[ft s^-1]
Cross-Section 2
ANSYS
v12.1

c)

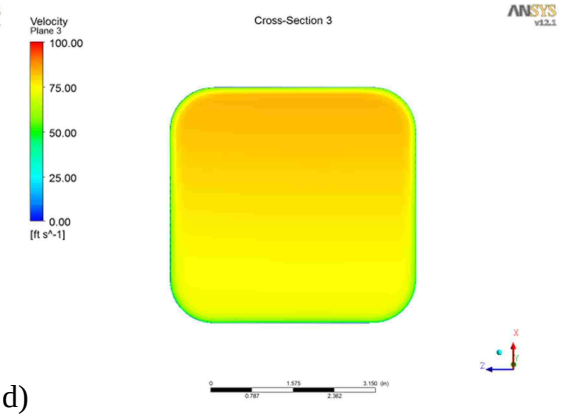
Velocity
Plane 3
100.00
75.00
50.00
25.00
0.00
[ft s^-1]
Cross-Section 3
ANSYS
v12.1

d)

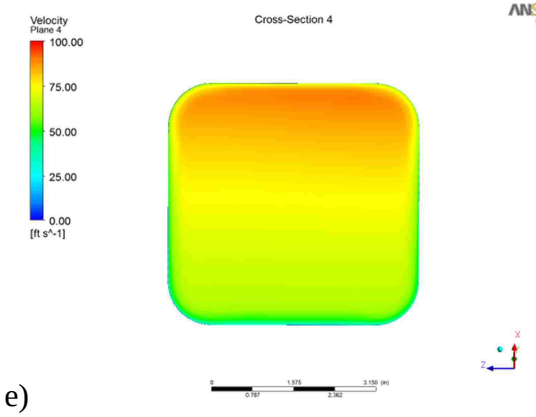
Velocity
Plane 4
100.00
75.00
50.00
25.00
0.00
[ft s^-1]
Cross-Section 4
ANSYS
v12.1

e)

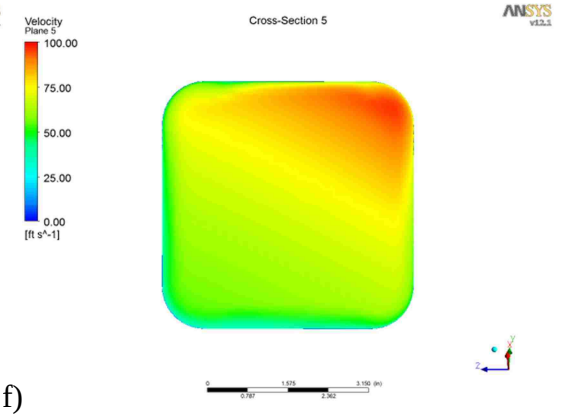
Velocity
Plane 5
100.00
75.00
50.00
25.00
0.00
[ft s^-1]
Cross-Section 5
ANSYS
v12.1

f)

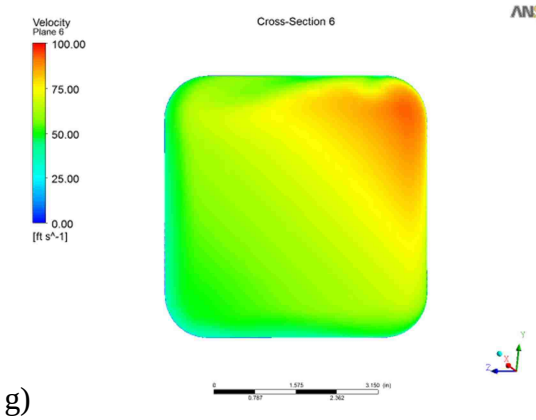
Velocity
Plane 6
100.00
75.00
50.00
25.00
0.00
[ft s^-1]
Cross-Section 6

g)

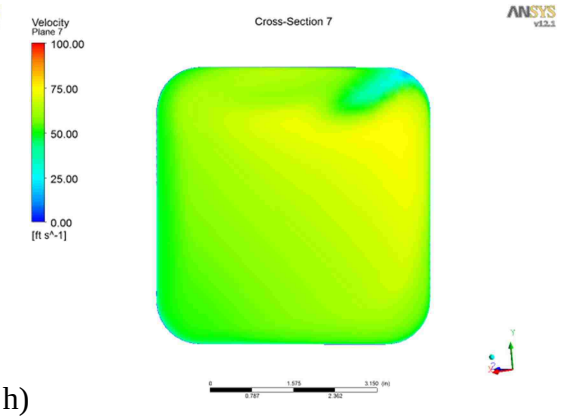
Velocity
Plane 7
100.00
75.00
50.00
25.00
0.00
[ft s^-1]
Cross-Section 7

h)

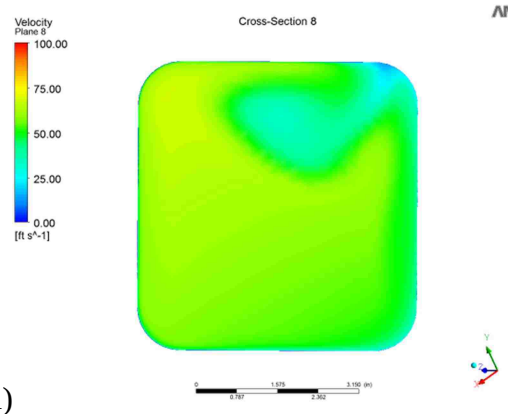
Velocity
Plane 8
100.00
75.00
50.00
25.00
0.00
[ft s^-1]
Cross-Section 8

i)

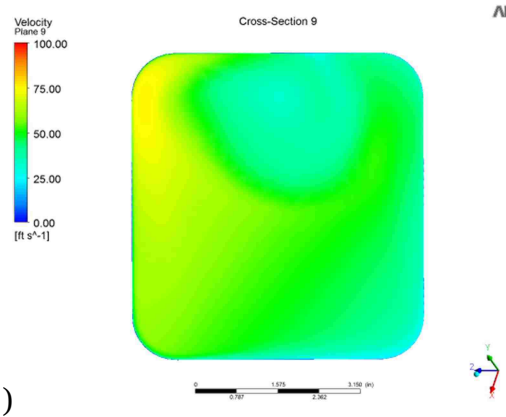
Velocity
Plane 9
100.00
75.00
50.00
25.00
0.00
[ft s^-1]
Cross-Section 9

j)

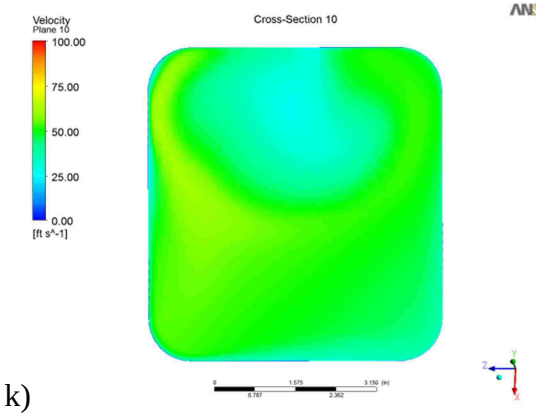
Velocity
Plane 10
100.00
75.00
50.00
25.00
0.00
[ft s^-1]
Cross-Section 10

k)

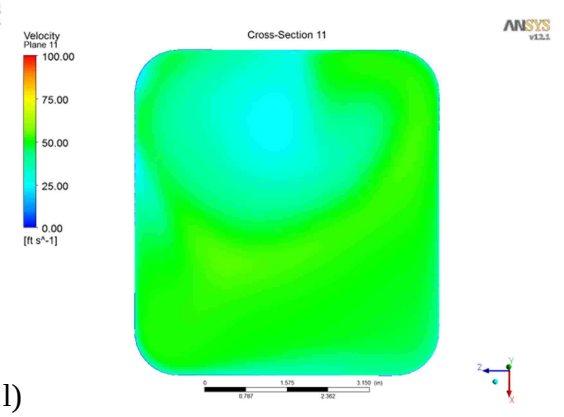
Velocity
Plane 11
100.00
75.00
50.00
25.00
0.00
[ft s^-1]
Cross-Section 11

l)

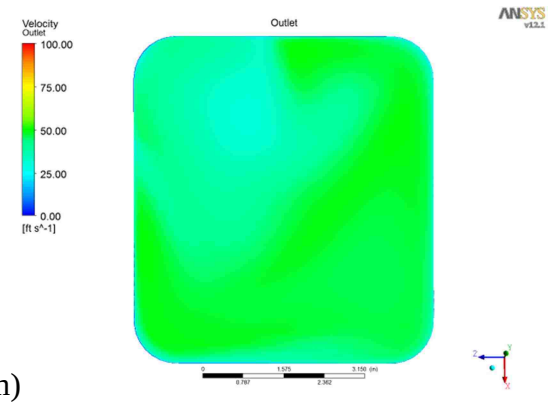


m)

**Figure 34 (a-m) - Cross-Sectional Velocity Contours from Inlet to Outlet**

The velocity vectors at the cross-sections can be used to further visualize the location and magnitude of the vortex tube passing through the crossover.

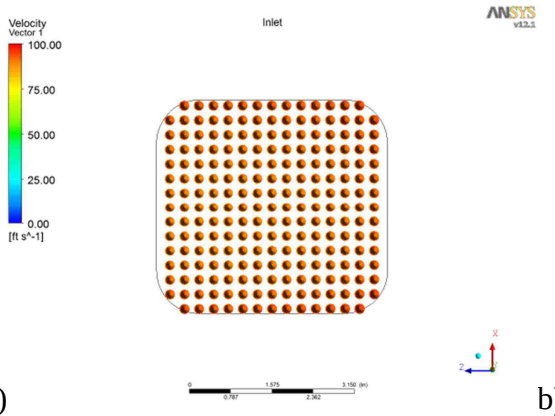


a)

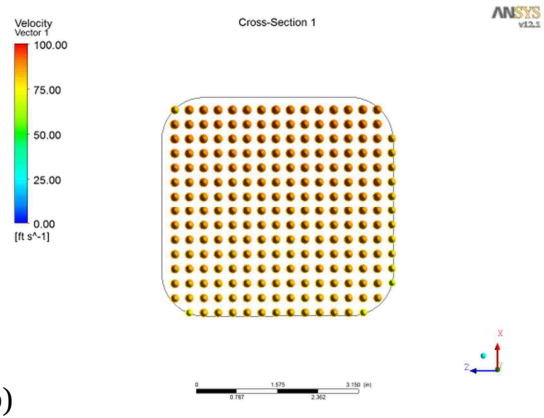


b)

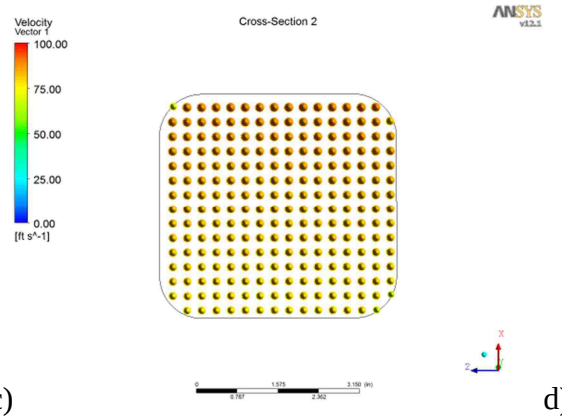


c)

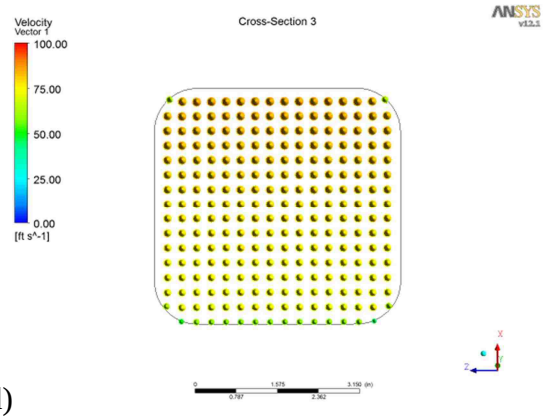


d)

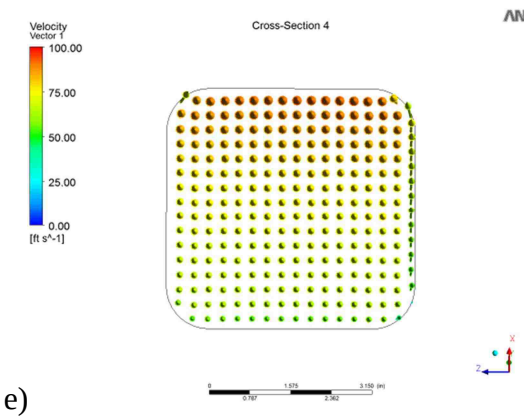
Velocity
Vector 1
100.00
75.00
50.00
25.00
0.00
[ft s^-1]
Cross-Section 4

e)

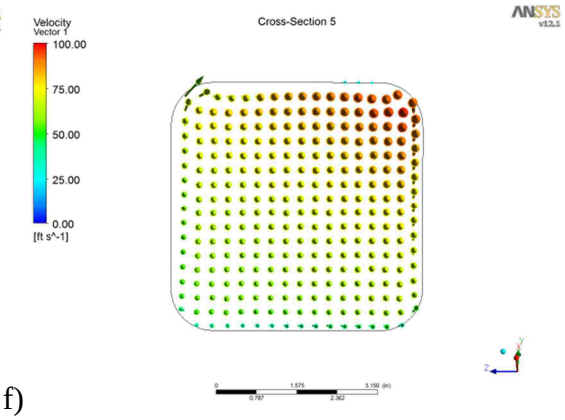
Velocity
Vector 1
100.00
75.00
50.00
25.00
0.00
[ft s^-1]
Cross-Section 5

f)

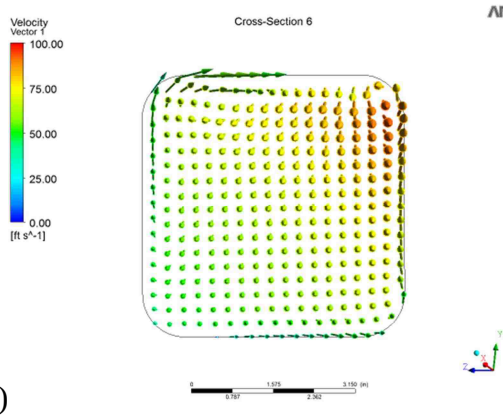
Velocity
Vector 1
100.00
75.00
50.00
25.00
0.00
[ft s^-1]
Cross-Section 6

g)

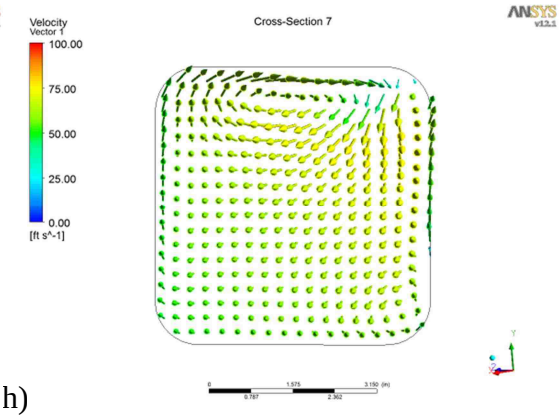
Velocity
Vector 1
100.00
75.00
50.00
25.00
0.00
[ft s^-1]
Cross-Section 7

h)

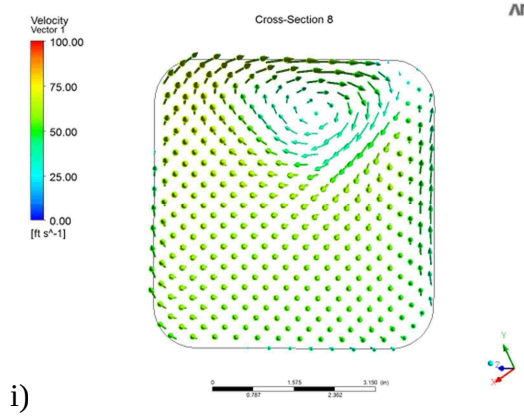
Velocity
Vector 1
100.00
75.00
50.00
25.00
0.00
[ft s^-1]
Cross-Section 8

i)

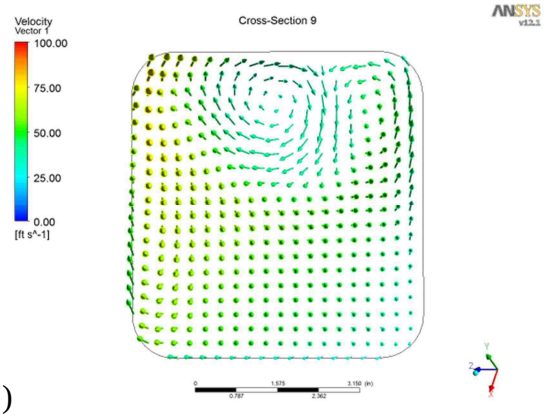
Velocity
Vector 1
100.00
75.00
50.00
25.00
0.00
[ft s^-1]
Cross-Section 9

j)

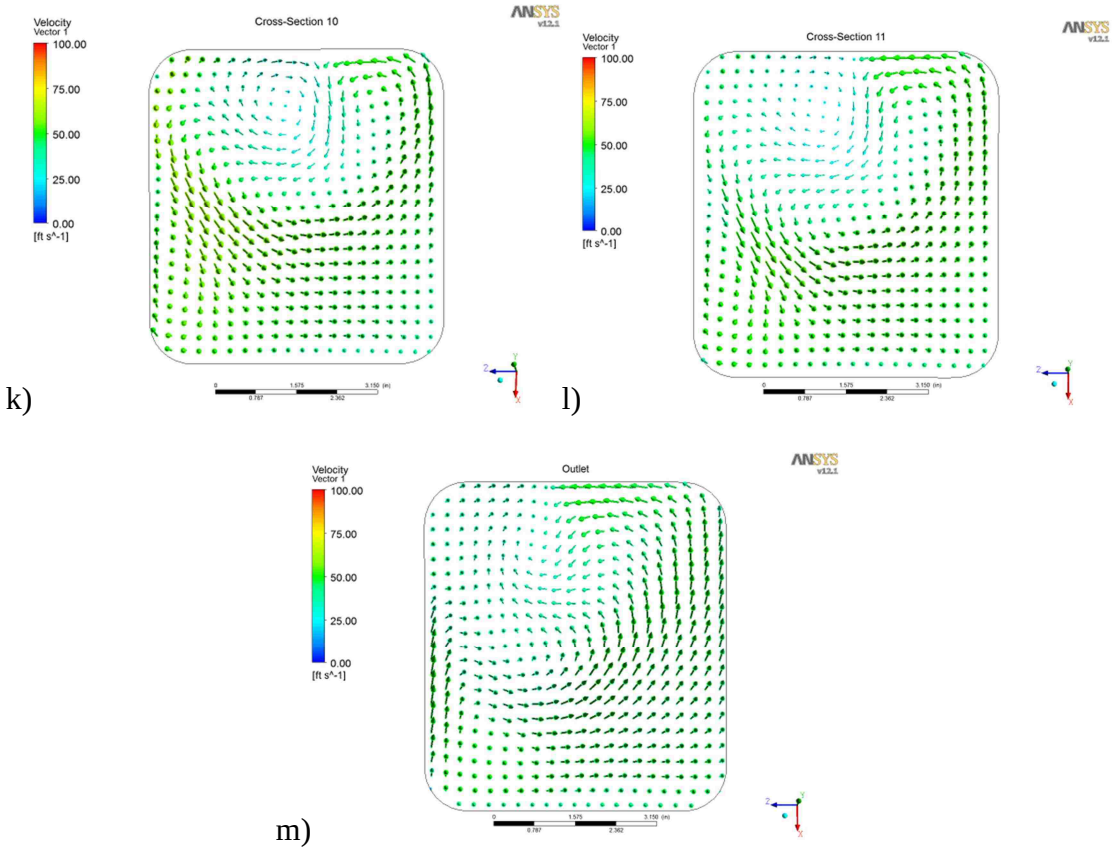


**Figure 35 (a-m) - Cross-Sectional Velocity Vector Plots from Inlet to Outlet**

Again, the flow can be seen to begin to swirl in earnest in the seventh cross-section. This swirl is carried across the inner path of the bend through the following cross-sections and then it is seen to migrate to the center of the passage in the last two cross-sections. This makes sense because the passage begins to straighten out, so the vortex tube should begin to migrate to the center as if it were in a straight tube.

## *3.4 Wall Shear*

A plot of the wall shear along the walls of the domain shows a very low value throughout the entire crossover.

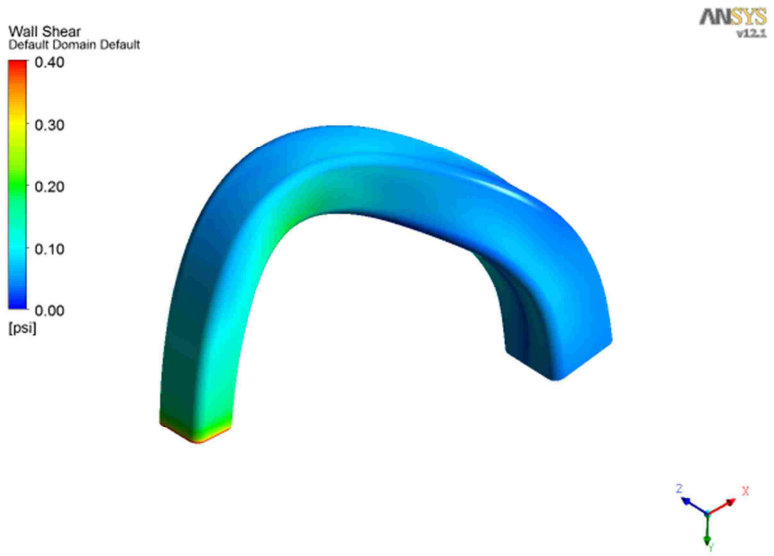


Figure 36 - Wall Shear Plot

The low shear area along the center of the inner bend of the outlet coincides with the vortex tube demonstrated by the velocity streamlines. The higher stress area midway along the first bend coincides with the beginning of the vortex tube.

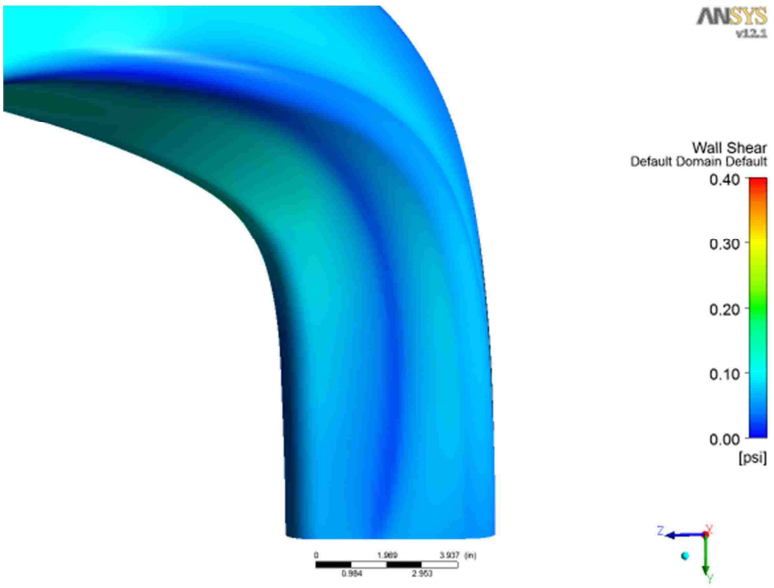


Figure 37 - Close-Up of Low Shear Area at Crossover Outlet

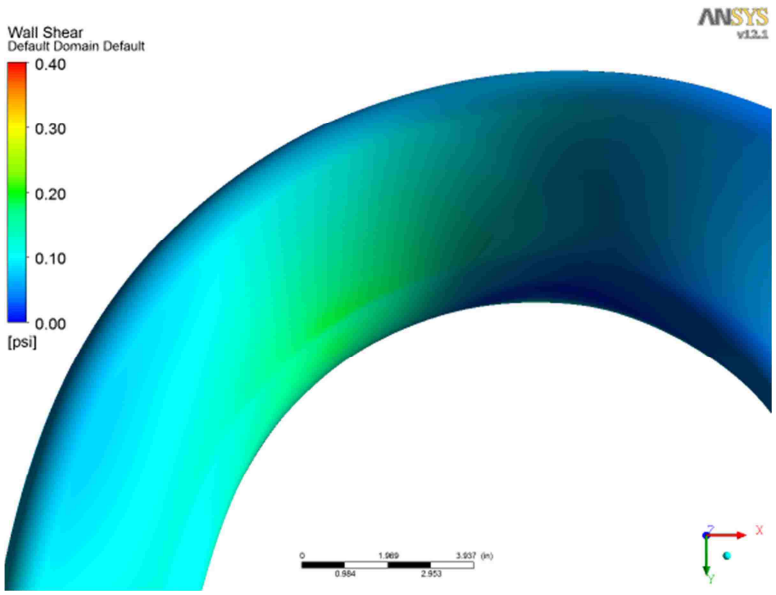


Figure 38 - Close-Up of High Shear Area in First Bend

Both of these shear areas are consistent with the theory for curved passages. The inner path of a bend is where the flow leaves the wall to travel along the middle of the passage to the outer path. This will leave a low shear area where the fluid leaves the wall due to the low transverse component of the velocity. The flow must also "ride" the boundary layer down the passage walls to replace the fluid leaving the wall at the inside of the bend. The shear, then, is expected to be higher along the walls as it circulates around the passage. Both of these phenomena are seen to exist in the simulated wall shear plot. It is also noted that the overall wall shear is quite low. This is consistent for a small static pressure change and a small mixing length; both of which are present in this domain due to the low hydraulic losses and turbulent flow.

# 4 Conclusions

The modified crossover passage was modeled and the flow simulated in order to quantify the hydraulic losses occurring in the geometry and to identify areas for improvement. Using CFD, the RANS equations were numerically solved utilizing the k-ε turbulence model. The results showed minimal losses through the passage and a potential area for improvement at the exit to minimize the secondary flow at the exit.

In conclusion, the new crossover design is seen to be exceptional, with only a 1.2% decrease in total pressure from the inlet to the outlet. The regions of low shear are on the inner paths of the bends, as expected. One would be hard-pressed to make any significant improvements on the geometric design in order to improve the flow characteristics. Furthermore, the velocity pressure only accounts for approximately 10% of the total pressure; thus any improvements in velocity pressure losses would have a negligible effect on the overall performance of the crossover.

The primary area of interest seems to be the flow pattern exiting the crossover. The amount of swirl being dumped into the suction volute for the succeeding impeller is rather high and can cause downstream problems affecting the hydraulic efficiency of the next impeller. Studies have shown that axisymmetric flow at the eye of the impeller is essential to smooth operation of a pump stage and significant energy has been expended by turbomachinery companies throughout the years in order to control this.

Further studies should be performed to document the effects that pump specific speed and size have on the crossover performance. Once this information is known, a program can be written to automatically generate the optimum crossover geometry for a given size, stage number, and specific speed.

The ability to automatically generate solid models of hydraulic passages would result in a significantly streamlined hydraulic design process with unprecedented lead times.

# 5 Bibliography

Ackroyd, J. e. (2001). *Early Developments of Modern Aerodynamics.* Oxford, UK: Butterworth-Heinemann.

ANSYS, Inc. (2009). *ANSYS CFD-Post Standalone: Reference Guide.* Canonsburg, PA: ANSYS, Inc.

ANSYS, Inc. (2009). *ANSYS CFX - Solver Theory Guide.* Canonsburg, PA: ANSYS, Inc.

ANSYS, Inc. (2009). *ANSYS CFX Solver Modeling Guide.* Canonsburg, PA: ANSYS, Inc.

Boussinesq, J. (1896). Théorie de l'Ecoulement Tourbillonnant et Tumultueux de Liquides dans les Lits Rectilignes à Grande Section. *Comptes Rendus de séances de l'Académie des Sciences, Vol. 122 (In French)*, 1290-1295.

Buckingham, E. (1915). On Model Experiments and the Form of Empirical Equation. *Trans. ASME, Vol. 37*, 263.

Cheney, W. (2004). *Numerical Mathematics and Computing, 5th Edition.* Belmont, CA: Brooks/Cole-Thomson Learning.

Douglas, J. F. (1979). *Fluid Mechanics.* London, UK: Pitman International.

Dunn, J. J. (2009). *On the Nature of the Flow in a Separated Annular Diffuser.* Orlando, FL: University of Central Florida.

Fox, R. W. (2004). *Introduction to Fluid Mechanics, 6th Edition.* Hoboken, NJ: John Wiley & Sons, Inc.

Gülich, J. (2010). *Centrifugal Pumps, 2nd Edition.* Heidelberg, Germany: Springer.

Karassik, e. a. (2008). *Pump Handbook, 4th Edition.* New York, NY: McGraw Hill.

Lobanoff, V. S., & Ross, R. R. (1992). *Centrifugal Pumps Design & Application, Second Ed.* Houston, TX: Gulf Publishing Company.

Miller, D. S. (1990). *Internal Flow Systems, 2nd Edition.* Cranfield, UK: BHRA (Information Services).

Pope, S. B. (2000). *Turbulent Flows.* Cambridge, UK: Cambridge University Press.

Prandtl, L. (1905). Über Flüssigkeits bewegung bei kleiner Reibung. *Verhandlungen des dritten internationalen Mathematiker-Kongresses (In German)* (pp. 484-491). Leipzig, Germany: Tuebner.

Stepanoff, A. (1993). *Centrifugal and Axial Flow Pumps, Second Ed.* Malabar, FL: Krieger Publishing Company.

White, F. M. (2003). *Fluid Mechanics, 5th Edition.* New York, NY: McGraw Hill.

Wilson, D. G. (1984). *The Design of High-Efficiency Turbomachinery and Gas Turbines.* Cambridge, MA: The MIT Press.

# 6 Appendix A – Solid Modeling

With the emergence of commercially available numerical simulation technology and less expensive computing hardware, solid modeling has become increasingly more important in the manufacturing industry. Computer simulations at nearly every step of the manufacturing process can be used to reduce lead times and prototyping costs. One thing these programs have in common, though, is the old axiom, “Garbage in, Garbage out.”

This being the case, the ability to create efficiently constructed solid models is one of the most important basic skills a design engineer can possess. The solid models created in design offices should be of a high enough quality to be used in simulations ranging from metal casting pour and cooling simulations, plastic injection mold flow and fill simulations, rotordynamics, structural analysis, fluid dynamics, and transient heat transfer. Below is the procedure used to create the three-dimensional geometry simulated in this simulation. The geometry was created in AutoDesk Inventor, but the modeling process is universal.

The long crossover is easily seen to be a curved passage with varying area along its sweep path. Once the engineering has been done for the area development and path, this function must be translated into a physical specimen. The two-dimensional drawings describe the path from the side view and the top view. Understanding how the coordinate systems for the two views are related (in this case a

90º rotation about the horizontal Y-axis) is instrumental in knowing how to place the reference points in Cartesian space. Figure 13 defines these reference points as being the intersection of the geometry's mean path line and a series of radial lines emanating from the pump shaft centerline. Designating the Z-axis as the rotating axis of the pump shaft, the X and Y coordinates can be measured directly from this view. Figure 14 displays the top view of the pump and uses the X coordinates from the side view to extrapolate the third dimension's value. Measuring the distance from the reference plane, in this case the impeller discharge centerline, a point table can be constructed to define the three-dimensional path of the crossover's mean path line (essentially its three-dimensional centerline).

These points are imported into Inventor and connected with a three-dimensional spline[2] function. It is important to include the points as selectable features so that the individual sections can be constructed about them.

[2] A spline function consists of several polynomial pieces joined together with certain smoothness conditions (Cheney, 2004).

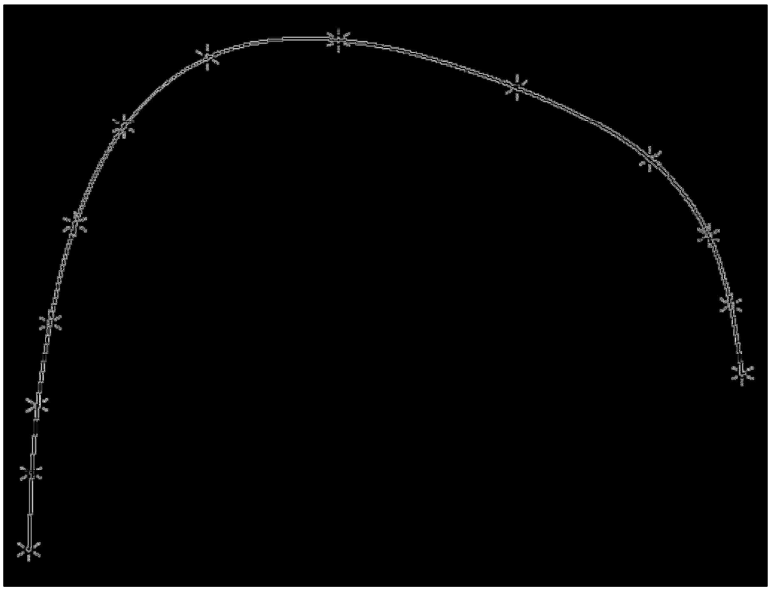

Figure 39 - 3-D Mean Path Line with Section Origin Points

With the mean path line and the section origins constructed, the individual section planes can be defined. These planes are defined by selecting the corresponding origin point and defining the plane's normal to be tangent to the mean path line at that point. This gives a series of planes that are continually changing direction so as to always "face" down the mean path line.

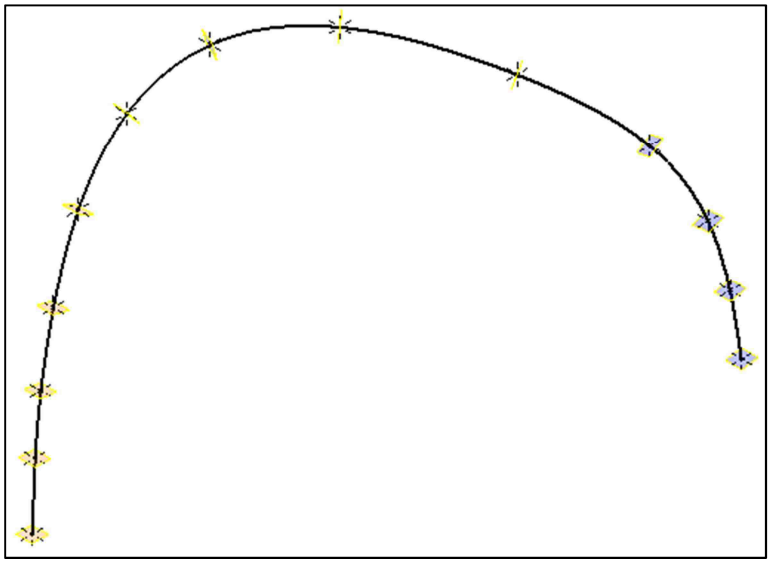

Figure 40 - Section Planes Along the Mean Path Line

Next, the individual sections are drawn so they can then define the cross-sections of the solid model.

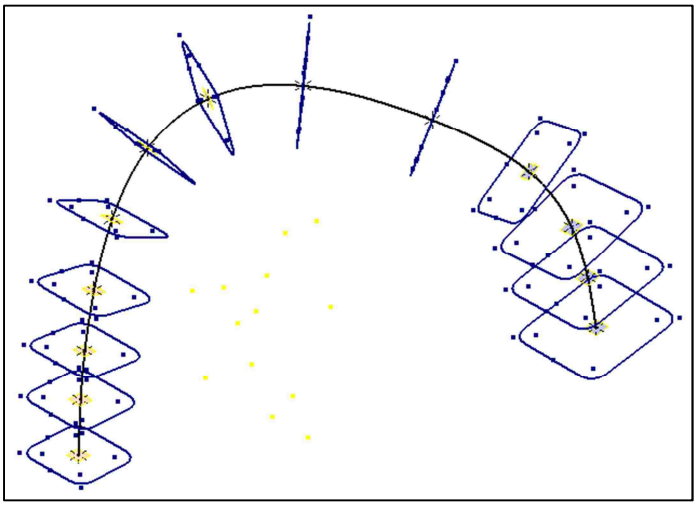

Figure 41 - Cross Sections for Solid Modeling Construction

Finally the cross-sections are chosen, in order, and a three-dimensional solid is generated that follows the mean path line and whose outer profile coincides with the cross-sections.

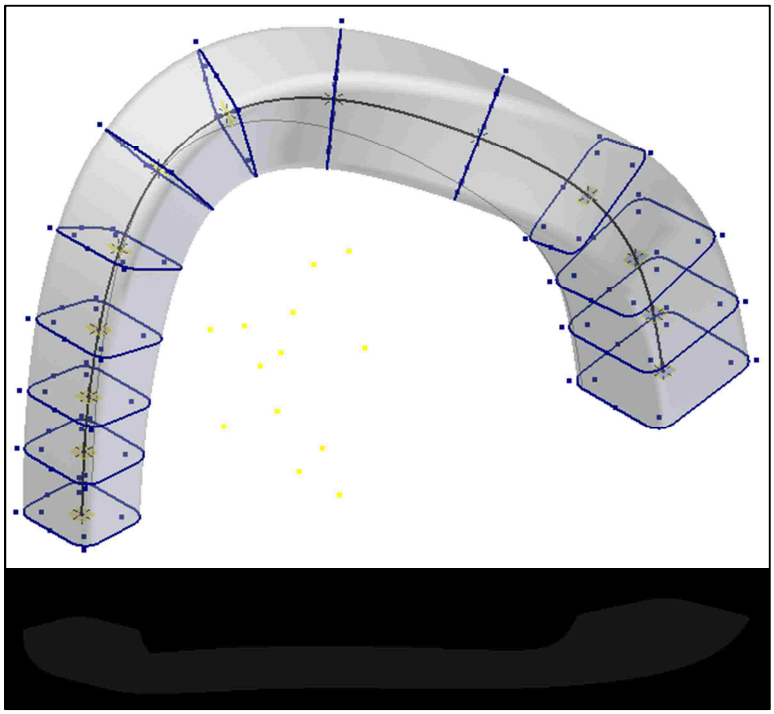

Figure 42 - Lofted Crossover Solid Model

Inventor is interoperable with ANSYS, which affords the user the ability to group various faces and designate them as named selections. It is good practice to name the different boundary regions that will be used in a simulation, that way it is assured that the proper region is used when designating inlets, outlets, and other pertinent boundary conditions. Another advantage to named selections is that different models can be constructed with significantly different geometry, but the same names. This way, different models can be parametrically compared to identify the optimum geometry for an application.

This model is very simple in that it has an easily identifiable inlet and outlet, but this may not be so apparent in larger complex models. Multi-branched piping systems are a good example of a type of model with several inlets and outlets. Also, most completed models will contain several faces, fillets, chamfers, and other features which are time consuming to select individually. A completed impeller model is a good example of a multi-surface model. The blade has wall fillets, the passage centerlines are the periodic boundaries, and the passage walls can be smooth or rough depending on the manufacturing process. Naming each of these regions allows the user to designate specific boundary conditions and surface roughness to large groups of faces more easily.

# 7 Appendix B – Turbulence Models

At heart, the Navier-Stokes equations account for all of the properties of a flow field. This means that, given the adequate mathematical techniques, turbulence can be directly solved using nothing more than these textbook non-linear partial differential equations. However, the Navier-Stokes equations have yet to be solved in a general fashion and they are not expected to be solved analytically in the foreseeable future.

This leaves the possibility of solving them numerically. Again, theoretically, a Direct Numerical Simulation (DNS) can be applied. The issue with this is that the length scales associated with turbulence range from the microscopic to several meters in length depending on the Reynolds number, geometry, forcing function, etc. It has been estimated that the computational cost of a DNS is proportional to $Re^3$ (Pope, 2000). Needless to say, commercially viable machines that can handle this type of simulation have yet to be developed and are not expected to be developed in the foreseeable future.

This leaves us with the question of how to model turbulent flow. A great deal of research has gone into developing and applying different turbulence models. The random, chaotic eddy formation and dissipation characteristic of turbulent flow is near impossible to capture using standard analytical methods. Add to this the fact that this behavior is somewhat Reynolds Number dependent and it is easy to see why it is such a problem for researchers everywhere.

## *7.1 History of Turbulent Modeling*

A turbulence model is a construct used to predict the turbulent behavior of flow. The first models used introduced the ideas of eddy viscosity, introduced by Boussinesq in 1896 (Boussinesq, 1896), and mixing lengths and boundary layers, introduced by Prandtl in 1904 (Prandtl, 1905). These two concepts are still the basis of more complex turbulence models in the modern era.

Boussinesq's eddy viscosity is added to the classically defined physical viscosity of a fluid. It is an empirically derived relationship which compensates for the added internal stresses in a fluid stream due to turbulence. An important characteristic of this relationship is that it is a property of the *flow* not the *fluid* (White, 2003). The first applications of this theory used constant values and are quite accurate for free shear flows such as axisymmetric jets.

Prandtl's boundary layer theory related the eddy viscosity to the distance of the flow from a solid wall and the change in tangential velocity in this boundary layer. This makes the local eddy viscosity high in the proximity of the solid wall and allows it to normalize to the free stream eddy viscosity approximated by Boussinesq as it approaches the mixing length. This is the historical foundation for our modern two-equation turbulence models. In its most simple form, the near-wall eddy viscosity, $\mu_t$, can be modeled as:

$$\mu_t \approx \rho l^2 \left|\frac{\partial U}{\partial y}\right|$$

Where *l* is the mixing length of the boundary layer and *y* is the perpendicular distance from the nearest wall. This approximation works extremely well for attached flows with low pressure gradients (White, 2003). Unfortunately, diffusors and other fluid motion control components have large pressure gradients, so more advanced turbulence modeling techniques had to be developed to handle more complex flows.

## *7.2 Development of the Reynolds Averaged Navier-Stokes (RANS) Equations*

The most common turbulence models are statistical turbulence models. These models make use of the fact that turbulent flow exhibits average characteristics with time scales that are much greater than those exhibited by the turbulent fluctuations. With this in mind, a turbulent flow can be said to have an average component and a time-varying component (ANSYS, Inc., 2009). This generalization leads to the derivation of the RANS equations.

The RANS equations divide the flow components into an averaged and fluctuating value such that a velocity, $U_i$, for example, can be represented by:

$$U_i(\vec{r},t) = \overline{U}_i(\vec{r}) + u_i(\vec{r},t)$$

Where $\vec{r}$ is the position vector and $\overline{U}_\iota$ can be defined as:

$$\overline{U}_i = \frac{1}{\Delta t}\int_t^{t+\Delta t} U_i dt$$

Substituting the averaged velocity into the Navier-Stokes equations, using Einsteinian notation, and dropping the bar for averaged values yields:

$$\frac{\partial \rho}{\partial t} + \frac{\partial}{\partial x_j}(\rho U_j) = 0$$

$$\frac{\partial \rho U_i}{\partial t} + \frac{\partial}{\partial x_j}(\rho U_i U_j) = -\frac{\partial P}{\partial x_i} + \frac{\partial}{\partial x_j}(\tau_{ij} - \rho\overline{u_i u_j}) + S_M$$

Where $\tau_{ij}$ is the molecular stress tensor:

$$\tau_{ij} = 2\mu S_{ij} = \mu\left(\frac{\partial U_i}{\partial x_j} + \frac{\partial U_j}{\partial x_i}\right)$$

The $\rho\overline{u_i u_j}$ term is what is known as the Reynolds stress. These are turbulent flux terms in addition to the molecular diffusive fluxes (ANSYS, Inc., 2009). The presence of these fluctuating components is due to the differentiation performed on the non-linear portion of the momentum equation. These are important for heat transfer because at high Reynolds numbers the length scales of these fluctuations is much greater than those associated with the mean free path of the thermal fluctuations. This makes the turbulent fluxes the dominant heat transfer method in very turbulent flow, which helps explain why turbulent flow is a better heating and cooling medium than laminar flow.

The above process can be applied to the Reynolds averaged transport equation for any additional non-reacting variable, Φ, which can be separated into an average term and a fluctuating term (ANSYS, Inc., 2009):

$$\Phi = \bar{\Phi}(\vec{r}) + \varphi(\vec{r}, t))$$

$$\frac{\partial \rho \Phi}{\partial t} + \frac{\partial}{\partial x_j}(\rho U_j \Phi) = \frac{\partial}{\partial x_j}\left(\left(\Gamma_\Phi + \frac{\mu_t}{\sigma_\Phi}\right)\frac{\partial \Phi}{\partial x_j}\right) + S_\Phi$$

Where $\Gamma_\Phi$ is the diffusivity of $\Phi$ and $S_\Phi$ is a source vector.

### *7.3 Handling the Reynolds Stress*

The RANS equations are a valuable tool in solving fluid dynamics problems, unfortunately there is no viable direct method of solving for the Reynolds stress terms. In order to handle this term and close the equation several models have been proposed. Of interest in this simulation are the k-ε and shear stress transport (SST) turbulence models. Both of these models fall into the category of eddy viscosity turbulence models.

Eddy viscosity turbulence models use the gradient diffusion hypothesis to relate the Reynolds stresses to the mean velocity gradients and the eddy viscosity. This hypothesis is analogous to the stress/strain relationship in laminar flow (ANSYS, Inc., 2009):

$$-\rho\overline{u_i u_j} = \mu_t\left(\frac{\partial U_i}{\partial x_j} + \frac{\partial U_j}{\partial x_i}\right) - \frac{2}{3}\delta_{ij}\left(\rho k + \mu_t \frac{\partial U_k}{\partial x_k}\right)$$

Where *k* is the flow's turbulent kinetic energy defined as the variance of the fluctuations in velocity.

Substituting this back into the RANS equations and making use of the definition of the mean strain rate tensor:

$$\frac{\partial \rho U_i}{\partial t} + \frac{\partial}{\partial x_j}\left(\rho U_i U_j\right) = -\frac{\partial p'}{\partial x_i} + \frac{\partial}{\partial x_j}\left[\mu_{eff}\left(\frac{\partial U_i}{\partial x_j} + \frac{\partial U_j}{\partial x_i}\right)\right] + S_M$$

Where $\mu_{eff}$ is the effective viscosity and *p'* is the modified pressure that includes the second term of the Reynolds stress:

$$\mu_{eff} = \mu + \mu_t$$

$$p' = p + \frac{2}{3}\left(\rho k + \mu_{eff}\frac{\partial U_k}{\partial x_k}\right)$$

The last term in the modified pressure above is a divergence term and can be neglected in incompressible fluids (ANSYS, Inc., 2009).

As Prandtl defined it, the turbulent viscosity is dependent upon the length scale it is being applied to. The dissipation of the turbulent eddies is also dependent upon a velocity scale. There are several approximations for these scales which can be directly substituted into the RANS, however, they are rigid relationships and do not adapt well to changing geometries and velocity profiles. As there are no adaptive properties that take the surrounding environment into account, these methods are called Zero Equation Turbulence models. Much more sophisticated models have been developed to handle the actual variations in the flow field more accurately. One subset of these methods is called the Two Equation Turbulence models. They are named this because

they introduce two transport equations to handle the length scale and velocity scale, respectively. Both the k-ε and k-ω (of which SST is a member) classes of turbulence modeling are Two Equation Turbulence models.

### *7.4 k-ε Model*

The k-ε model uses two new variables to define the turbulent viscosity; k is the turbulence kinetic energy and ε is the turbulent eddy dissipation (ANSYS, Inc., 2009). The relationship between the turbulent viscosity, $\mu_t$, and the new variables is:

$$\mu_t = C_\mu \rho \frac{k^2}{\varepsilon}$$

Where $C\mu$ is a constant (see Table 2). k and ε are then derived from the Reynolds averaged transport equation as:

$$\frac{\partial \rho k}{\partial t} + \frac{\partial}{\partial x_j}(\rho U_j \mathrm{k}) = \frac{\partial}{\partial x_j}\left(\left(\mu + \frac{\mu_t}{\sigma_\mathrm{k}}\right)\frac{\partial \mathrm{k}}{\partial x_j}\right) + P_\mathrm{k} - \rho\varepsilon + P_{kb}$$

$$\frac{\partial \rho \varepsilon}{\partial t} + \frac{\partial}{\partial x_j}(\rho U_j \varepsilon) = \frac{\partial}{\partial x_j}\left(\left(\mu + \frac{\mu_t}{\sigma_\varepsilon}\right)\frac{\partial \varepsilon}{\partial x_j}\right) + \frac{\varepsilon}{k}(C_{\varepsilon 1} P_\mathrm{k} - C_{\varepsilon 2}\rho\varepsilon + C_{\varepsilon 1} P_{\varepsilon b})$$

The $P_{kb}$ and $P_{\varepsilon b}$ terms above are from the buoyancy forces and the $P_k$ term is turbulence due to viscous forces. The rest of the undefined parameters are constants summarized below in Table 2.

| | | |
|---|---|---|
| $C_{\varepsilon 1}$ | k-ε turbulence model constant | 1.44 |
| $C_{\varepsilon 2}$ | k-ε turbulence model constant | 1.92 |
| $C_{\mu}$ | k-ε turbulence model constant | .09 |
| $\sigma_k$ | Turbulence model constant for the *k* equation | 1.0 |
| $\sigma_{\varepsilon}$ | k-ε turbulence model constant | 1.3 |

**Table 2 - k-ε Turbulence Modeling Constants (ANSYS, Inc., 2009)**

There has been much discussion as to which turbulent model is the most appropriate for analyzing flow in curved passages. Gülich lists several weaknesses of this model (Gülich, 2010):

- Flows on curved paths
- Decelerated flows
- 3-D boundary layers
- Rotating components
- Swirling flows
- Strong secondary flows
- Secondary flows induced by turbulence cannot be captured (encountered in channels with non-circular cross-sections
- Production of turbulent kinetic energy is over-predicted in locations with strong velocity gradients

It is easily noted that every one of these weaknesses applies to pumps and over half of them to the long crossover in particular. The k-ε method was used,

nonetheless, because of the small difference in predicted head loss from the SST method (which is computationally more expensive). The wall function assumed in this model is sufficient to generate similar results to the more accurate SST method while taking less time to finish. This is most likely due to the protracted nature of the diffusion in the passage. The area ratio of the redesigned long crossover is constantly increasing over a total distance of more than a meter, resulting in a very small, gradual growth rate. The section areas are of an order of $10^4$ $mm^2$, so the diffusion rate is negligible in the crossover although the end result is a more than twofold increase in area.

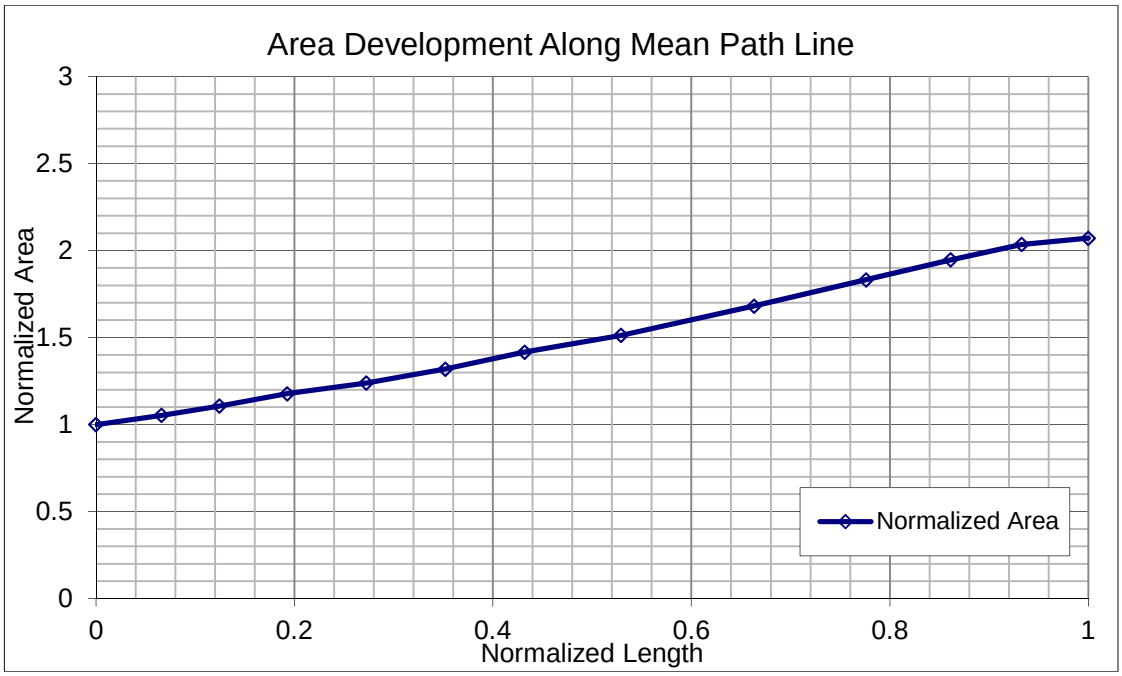


Figure 43 - Normalized Area Development

The changes implemented from the original long crossover design actually tend to diminish the areas that would otherwise give rise to problems in utilizing the k-ε turbulence model.

Despite the weaknesses inherent in the method, k-e remains a popular turbulence modeling method because it is the oldest Two Equation Turbulence model available. Thus it has a broad validation basis (Gülich, 2010). Modern versions of the k-ε model have been developed to address the shortcomings mentioned above, but they still employ a logarithmic wall function. This imposes a specific flow at a solid wall rather than letting the flow develop as naturally as possible within the simulation. Regardless, the k-ε model is still accurate for the core flow and highly convergent due to its wall function. It can be used with some degree of caution for flows where inertial effects outweigh the friction effects (i.e. high Reynolds number).

### *7.5 k-ω & SST Model*

The k-ω model was developed specifically for flows against strong pressure gradients such as those seen in diffusors. The transport equation uses a turbulent viscosity related to the frequency, $\omega$, of relatively large vortices (ANSYS, Inc., 2009):

$$\mu_t = \rho \frac{k}{\omega}$$

This model does not require the non-linear damping functions required by the k-ε method, making it more accurate and robust (albeit more computationally expensive).

ANSYS contains multiple k-ω turbulence models. The method of interest to this analysis is the Shear Stress Transport (SST) method. This model accounts for the transport of turbulent shear stress and gives highly accurate predictions of the onset and the amount of flow separation under adverse pressure gradients (ANSYS, Inc., 2009).

The SST method applies a limiter to the kinematic eddy viscosity, $v_t$, according to the formulation (ANSYS, Inc., 2009):

$$v_t = \frac{\mu_t}{\rho} = \frac{a_1 k}{max(a_1\omega, SF_2)}$$

Where S is an invariant measure of the strain rate, $a_1$ is equal to $5/9$, and $F_2$ is a blending function (ANSYS, Inc., 2009):

$$F_2 = tanh(arg^2)$$

$$arg = max\left(\frac{2\sqrt{k}}{\beta'\omega y}, \frac{500v}{y^2\omega}\right)$$

Where $v$ is the kinematic viscosity and $\beta'$ is a model constant equal to .09.

The blending function is critical to the success of this method because this method is not valid for the core flow. $y$ is the distance from the nearest wall, so as the nodes get further from the wall, the blending function decreases. Once the nodes are far enough away, the turbulent viscosity simply becomes the original definition outlined for the k-ω method.

The SST method also tracks a variable known as the wall scale. This variable is the distance from the nearest wall which the transition from the k-ω to k-ε takes place (ANSYS, Inc., 2009). In other words, it is used by the various functions that control the transition from the near wall to free stream turbulence models in a manner analogous to Prandtl's mixing length for eddy viscosity as a function of the distance from a wall. This distance is derived by taking the Poisson's equation for a given variable[3], $\varphi$:

$$\frac{d^2\varphi}{dy^2} = -1$$

Where $\varphi = 0$ at the wall ($y = 0$).

Integrating twice yields:

$$\varphi = -{}^1\!/_2\, y^2 + C_1 y + C_2$$

Applying the boundary condition and noting that $\frac{d\varphi}{dy} = -y + C_1$ yields:

$$\varphi = {}^1\!/_2\, y^2 + y\frac{d\varphi}{dy}$$

This can be rearranged into a quadratic equation of $y$:

$${}^1\!/_2\, y^2 + \frac{d\varphi}{dy} y - \varphi = 0$$

[3] The outlined derivation and three-dimensional generalization are taken from the ANSYS-CFX documentation (ANSYS, Inc., 2009).

Solving and taking the positive root (because the flow is on the positive side of the wall) yields:

$$y = -\frac{d\varphi}{dy} + \sqrt{\left(\frac{d\varphi}{dy}\right)^2 + 2\varphi}$$

This process can also be generalized to three dimensions by:

$$\nabla^2\varphi = -1$$

Applying Dirichlet conditions of $\varphi = 0$ at the walls and Neumann conditions (i.e. zero flux) on the free stream boundaries will yield the generalized wall scale function:

$$Wall\ Distance = -|\nabla\varphi| + \sqrt{|\nabla\varphi|^2 + 2\varphi}$$

In the case of the SST model, the variable of interest would be the large vortex frequency, ω, used to define the turbulent viscosity. This makes sense because near the wall inside the laminar viscous boundary layer, the eddy frequency would go to zero due to the absence of turbulence. Away from the wall the frequency would tend towards the free-stream turbulence, which would be a constant value dependent on Reynolds number. Thus the k-ω methodology of resolving the turbulent viscosity would apply within this region defined by the wall distance bounding the layer of flow with changing vortex frequency:

$$Wall\ Distance = -|\nabla\omega| + \sqrt{|\nabla\omega|^2 + 2\omega}$$

In the flow beyond this mixing length, the frequency is considered constant throughout the free-stream. It can be assumed that the eddy dissipation is a function of the vortex frequency because the velocities and kinetic energy levels of physical systems in motion change linearly with the frequency of that motion. If the frequency is no longer changing, there is one less variable defining the eddy dissipation in the free-stream. Without needing to account for the effects of a changing vortex frequency, a simpler turbulence model can be used. It now becomes acceptable to exchange computational efficiency for rigorous flow simulation and the k-ε turbulence model is employed for the rest of the flow.

# 8 Vita

Alex Hernandez was born in Los Angeles, California on April 24, 1979 to Daniel and Maria Hernandez. He grew up with his two siblings, Jason and Amanda, in California and Nevada, where he worked as a journeyman toolmaker at Astro Mold for ten years. He did his undergraduate and graduate studies at Lehigh University. Alex has worked as a hydraulics engineer at Flowserve Corporation since 2007.